Thiol-rich and ion-imprinted alginate hydrogel as a highly adsorptive and recyclable filtration membrane for rapid and selective Sr(II) removal

Botuo Zheng[#,a], Jiajia Yin[#,a], Lingdan Zhu[a], Bingnan Zhou[a], Hang Shen[b], David Harbottle[c], Timothy N. Hunter[c], Yu Sheng[a], Deqin Zhu[a], Huagui Zhang[a,d,*]

[a] College of Chemistry and Materials Science, Fujian Key Laboratory of Polymer Materials, Fujian Normal University, Fuzhou 350007, China

[b] College of Materials and Chemical Engineering, Minjiang University, Fuzhou 350108, China

[c] School of Chemical and Process Engineering, University of Leeds, Leeds LS2 9JT, United Kingdom

[d] Institute of Physical Chemistry, RWTH Aachen University, Landoltweg 2, Aachen 52056, Germany

Abstract

Radioactive metal ion such as strontium ion, $^{90}Sr^{2+}$, has posed severe threats to environments and humans since the wide application of nuclear power plants around the world, while a rapid remediation of Sr^{2+} contaminated water still remains challenging. The current study developed an economical biomaterial-based hydrogel adsorbent with excellent Sr^{2+} adsorption performance achieved by ion-imprinting and abundant thiol groups, which was adaptable as an adsorptive filtration membrane for efficient and rapid purification of Sr^{2+} polluted water.

The hydrogel was synthesized via a three-step route based on sodium alginate (SA). First, SA was emulsified and converted via Sr^{2+} complexation to hydrogel (SA-Sr); secondly, a thiol-rich carboxyethyl grafted pentaerythritol tetrakis (thioglycolic acid) ester (PA) synthesized by click chemistry was used to covalently crosslink the hydrogel (SA-PA-Sr) with abundant thiol groups simultaneously introduced. Lastly, a Sr^{2+}-imprinted adsorbent (SA-PA-H) was obtained via acid elution of the SA-PA-Sr gel.

The SA-PA-H was demonstrated to exhibit a superior Sr^{2+}adsorption capacity (~151.7 mg/g), a rapid adsorption kinetics following pseudo-second order with a rate constant of 0.669 g mg^{-1} min^{-1}, decent selectivity for Sr^{2+}, a value ~ 1.14×10^{3} mL g^{-1} when adsorbing 10 ppm Sr^{2+} from

concentrated (100 ppm) solutions of competitive ions (Na^+ or Mg^{2+}). The good performance was maintained over a wide range of pH (4-10) and temperature (25-40 °C), and the adsorption mechanism was attributed to the prevalent Sr^{2+} bindings to thiol groups and Sr^{2+}-imprinted cavities. Moreover, high elasticity with a storage shear modulus ~ 10 MPa at low strains whilst rapid and full self-recovery after being repeatedly damaged by large strains of the SA-PA-H were demonstrated by rheology. This allowed the SA-PA-H to be adapted as a membrane for vacuum filtration, giving a high removal efficiency (> 99.2%) of Sr^{2+} under a high liquid flux (~ 40 L m^{-2} h^{-1}). In addition, the adsorbent can be regenerated by acid washing and after four consecutive adsorption-desorption cycles, the drop in removal efficiency was minor (53.51% to 36.88% for 100 ppm Sr^{2+}). This investigation demonstrated a novel hydrogel adsorbent advantageous in cost, performance, processability, and sustainability, being applicable for rapid and complete decontamination of nuclear wastewater via adsorptive membrane filtration.

Keywords Ion-imprinting; alginate; strontium; adsorption; thiol; membrane; hydrogel

1 Introduction

^{90}Strontium (^{90}Sr) is one of the major products of nuclear fission, possessing a long half-life (28.79 years) with high energy β-decay. Moreover, its cation, i.e. $^{90}Sr^{2+}$, is highly soluble in water. Hence, if released, $^{90}Sr^{2+}$ poses severe threats to the environment and human bodies.[1] Due to its similar chemical properties to calcium, Sr^{2+} is prone to enrich in human bodies, especially in bones. The good affinity of $^{90}Sr^{2+}$ to bones prevents it from being excreted by metabolism like other poisons. It was demonstrated that people suffered from obvious risks of osteosarcoma, soft tissue cancer and leukemia when exposed to radioactive ^{90}Sr.[2] With the wide application of nuclear power around the world, how to treat polluted water containing radioactive ions including $^{90}Sr^{2+}$ has become an urgent problem. On the other hand, Sr and its derivatives are important metal materials and have been widely used in ceramics, coatings, electronics and pharmaceutics.[3-7] Development of efficient approaches to separating and recovering Sr^{2+} from polluted water not only protects humans and the environment but also generates significant economic benefits.

Researchers have developed several methods to separate metal ions from polluted water, such

as chemical precipitation,[8] extraction[9], floatation[10, 11], adsorption[11-14] and ion exchange[15, 16]. The methods have different removal efficiency and application scenes according to their mechanism. Among them, adsorption is considered to be one of the best ways to recover Sr^{2+} with high efficiency and various adsorptive materials are developed for the enrichment and separation of Sr^{2+}.[17-21] For example, graphene oxide which has a large specific surface area and oxygen functional groups is a good candidate for ion adsorption materials. Abu-Nada reported graphene oxide as a Sr^{2+} adsorbent in the aqueous system, with a maximum strontium adsorption capacity of 131.4 mg/g achieved.[22] Nevertheless, the traditional adsorbents for Sr^{2+}, such as polyantimonic acid,[23] sodium titanate[24] and zeolite[25-27], and nanocarbon materials[28], etc., are often prepared in form of powder with a tiny particle size (mostly in nanoscale or submicron scale), hence may cause secondary pollution when applied in water since the separation of the adsorbents are laborious. It is also difficult for the powdery adsorbents to be shaped to fit purification devices. Even though the adsorbents can be loaded to a matrix to improve their recovery abilities from water,[29, 30] the adsorption efficiency including maximum adsorption and adsorption rate generally decreases due to the loss of active adsorption sites. The relatively high cost of the adsorbent synthesis also limits its massive application. For this reason, the development of highly efficient, environment-friendly, and economical adsorbents for Sr^{2+} has attracted growing attention in the water treatment field.

Organic polymers usually have good stability and are easy to be functionalized by modification of monomer or polymer products. The shape of polymer adsorbent can also be tailored by various preparation techniques. The advantages have made polymers ideal candidates for adsorbents. For instance, Huh et al. synthesized a microporous covalent triazine polymer and loaded magnetite Fe_3O_4 nanoparticles on it.[31] The nanocomposite served as an efficient adsorbent for the removal of strontium ion (Sr^{2+}) from seawater with a maximum adsorption capacity of 128 mg/g. Wang et al. prepared polyaniline-functionalized porous chitosan grafted by polyacrylamide bearing sulfonic acid group and used it as Sr^{2+} adsorbent.[32] The maximum adsorption capacity was determined to be 88.95 mg/g. However, there are at least two main drawbacks hampering the wide application of polymer adsorbents. One lies in that the introduction of functional groups into polymer adsorbent for adsorption often involves extra tedious steps

during the synthesis of the polymers. Another is that a majority of polymers are known to be hard to degrade due to their carbon skeleton, that is, the commonly argued issue of the non-sustainability of plastics. To overcome the problem, bio-based polymer materials such as sodium alginate (SA) have been adopted as the matrix or the core adsorptive material to prepare biodegradable ion adsorbents. SA is a bio-derived polysaccharide, possessing the advantages of abundant sources, low cost, nontoxicity, and biodegradability, etc.[33, 34] SA is an excellent adsorbent for various metal ions because of abundant carboxylic side groups.[35-39] However, there is minor ion selectivity of SA towards specific ions like Sr^{2+}, which calls for further modification of SA to meet the requirement for water treatment.

In recent years, ion-imprinting was raised as a prominent technique to construct ion-responsive materials with selectivity to certain ions.[40] In typical ion-imprinting, the ion was first introduced as templates to complex with ligand groups in polymers. After the formation of the ion complex, crosslinking reactions were introduced via other groups on polymers to fabricate stable networks and fix the relative position of functional groups. By removing metal ions, cavities with precise shapes, sizes, and charge distribution conformed to the ion are readily created in the network. The cavities served as identification sites for the ion and thus endowed the polymer matrix with ion selectivity, which allowed the polymer to serve as an efficient adsorbent for the specific ion[41-43]. As an example of strontium recovery, Deng et al. reported a Sr^{2+}-imprinted alginate microsphere adsorbent,[44] which can successfully separate Sr^{2+} in oilfield water from other ions with a maximum adsorption capacity of 177.37 mg/g, but its microsphere form and un-crosslinking structure still make the adsorbent difficult to be recovered and unstable to be re-used.

Incorporating functional group with distinct affinity to the ion into the adsorbent is another effective strategy to enhance ion selectivity. Based on hard and soft Lewis acids and bases (HSAB) theory,[45] soft Lewis bases with large radii and highly deformable electron clouds are prone to combine with soft Lewis acids with similar properties. As a third-period element, sulfur was a soft Lewis base with a large radius and a thick electron cloud. Therefore, sulfur will preferentially combine with soft Sr^{2+} instead of other hard ions in a mixture of alkali and alkaline-earth metal ions including Na^{+}, Mg^{2+}, Ca^{2+}, and Sr^{2+}. Taking advantage of the feature, metal sulfides were demonstrated to be efficient adsorbents for Sr^{2+} and other soft metal ions such as Ba^{2+}, Co^{2+} and

Ni^{2+}.[46-48] Zhang et al. synthesized Na/Zn/Sn/S (NaZTS) quaternary metal sulfide nanosheets for efficient adsorption of radioactive strontium ions.[49] NaZTS exhibited ultrafast kinetics with an equilibrium time of 5 min, a broad active pH range (a removal rate of >98.4%), and a very low Sr^{2+} desorption (< 0.04%) when employed as Sr^{2+} adsorbent in aqueous solution. The outstanding ability of NaZTS to capture Sr^{2+} ions was attributed to ion exchange and strong Sr-S bonding following the HSAB theory. The introduction of sulfur functional groups such as sulfonic acids[50], sulfonates[51] and thiols[44] to the adsorbent is a promising way to prepare Sr^{2+}-selective adsorbents. Nevertheless, the traditional sulfur-containing inorganic compounds have fixed shapes and inherent brittleness, which make them difficult to be shaped and to accommodate different purification devices.

In this study, both the HSAB strategy and the ion-imprinting strategy were employed to develop a SA-based hydrogel adsorbent rich in thiol groups and owning Sr^{2+}-imprinted cavities to enhance the adsorption performance and selectivity. The Sr^{2+}-imprinted cavities were introduced by first using Sr^{2+} to complex the carboxyl groups of SA chains, whereby SA chains were networked and thus a SA hydrogel (SA-Sr) was produced, and then ion-imprinted cavities can be obtained if the Sr^{2+} were eliminated. However, the elimination of the Sr^{2+} crosslinks would completely destroy the hydrogel structure. To avoid this, as well as to introduce abundant thiol groups, a thiol-functionalized tetra-arm carboxylic crosslinker PA was synthesized and used to covalently crosslink the SA-Sr hydrogel through *in situ* esterification, before the Sr^{2+} being removed by acid elution to obtain a robust Sr^{2+}-imprinted hydrogel (SA-PA-H). The fabrication and structure characterization of the SA-PA-H hydrogel was fully validated via a series of techniques, and its adsorption performance of Sr^{2+} was evaluated in terms of isothermal adsorption, effect of competitive ions, time, pH and temperature, etc. Moreover, the robustness of the SA-PA-H hydrogel was assessed by rheology, and its application as adsorptive membranes for device filtration, together with its regeneration potentials were also assessed.

2 Experimental

2.1 Chemicals

Pentaerythritol tetrakis(mercapto acetate) (90%, PET4A), strontium chloride hexahydrate

(99.5%, $SrCl_2 \cdot 6H_2O$), dioctyl sodium sulfosuccinate sodium (96%, AOT), benzoin dimethyl ether (99%, DMPA) and sodium alginate (90%, SA) were purchased from Macklin. Acrylic acid (AA, ≥ 99%), concentrated hydrochloric acid (36.0-38.0%), sulfuric acid (95.0-98.0%) and dichloromethane were purchased from Sinopharm Chemical Reagent Co Ltd. All the reagents were used as received.

2.2 Synthesis

2.2.1 Synthesis of thiol group-functionalized carboxylic modifier PA

PET4A (6.0076 g, 13.89 mmol), and acrylic acid (2.25 g, 31.2 mmol) were dissolved in 40 mL dichloromethane followed by an addition of DMPA (0.3965 g, 1.547 mmol) as the photoinitiator. The solution contained in a round flask equipped with a water condenser was stirred and exposed to continuous UV light (250-420 nm) for 2 h. The reaction (Scheme 1) generated a mixture of PET4As functionalized with 1, 2, 3, or 4 carboxylic groups. The product was named PA and used in the following steps without further refinement.

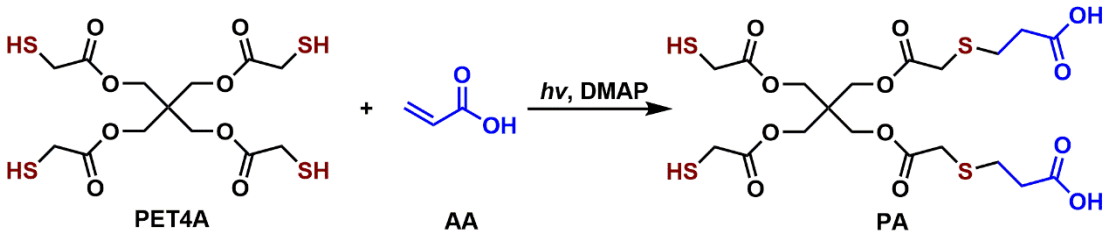

Scheme 1. Synthesis of PA from photo-initiated click reaction between PET4A and acrylic acid. A typical product with two thiol groups participating in the reaction is illustrated.

2.2.2 Preparation of Sr^{2+} complexed sodium alginate (SA-Sr) hydrogel

SA (1 g) was dissolved in 100 mL ultrapure water under stirring for 3 h to prepare a homogenous and viscous SA solution in a flask for further use. AOT surfactant (1.25 g) was dissolved in 50 mL dichloromethane followed by the addition of 25 mL of the as-prepared SA aqueous solution (1 wt%). The mixture was ultrasonicated using a Sonic Dismembrator (BILON-650Y) to prepare a W/O emulsion. Under stirring, 25 mL Sr^{2+}(0.5 wt% in water) was added dropwise and solid hydrogels precipitated from the emulsion. The mixture was stirred for 24 h to ensure full chelation between SA and Sr^{2+}, which generated an SA-Sr hydrogel. Then the emulsion

was centrifuged at 1000 rpm for 10 min to collect the hydrogel from the liquid and washed with ultrapure water repeatedly to remove excess Sr^{2+}.

2.2.3 Fabrication of PA crosslinked and Sr^{2+}-imprinted composite hydrogel (SA-PA-H)

About 10.0 g of the as-prepared swollen SA-Sr hydrogel (solid content 0.25 g) was re-dispersed in 20 mL ultrapure water followed by the addition of 20 mL dichloromethane solution of 4.0 g PA. 1.6 mL H_2SO_4 (0.5 wt%) was added dropwise to catalyze the esterification between the hydroxyl groups in SA and the carboxyl groups in PA (Figure 1). After stirring for 24 h, the chemically crosslinked hydrogel, named SA-PA-Sr, was fabricated and washed with ultrapure water three times and separated by centrifugation at 1000 rpm for 10 min. Thereafter, the Sr^{2+} previously chelated in the hydrogel was removed by dispersing SA-PA-Sr hydrogel in 50 mL hydrochloric acid (0.5 mol/L). The dispersion was stirred for 24 h and then washed with ultrapure water 3 times. The composite hydrogel product named SA-PA-H was obtained with a yield of 0.197 g (solid content) and 37.2%, assuming that two monosaccharide units chelating with one Sr^{2+} was crosslinked by one PA molecules and Sr^{2+} was completely removed by acid wash. The obtained SA-PA-H hydrogels were stored in swollen state in deionized water before use. The synthesis procedure is illustrated in Figure 1.

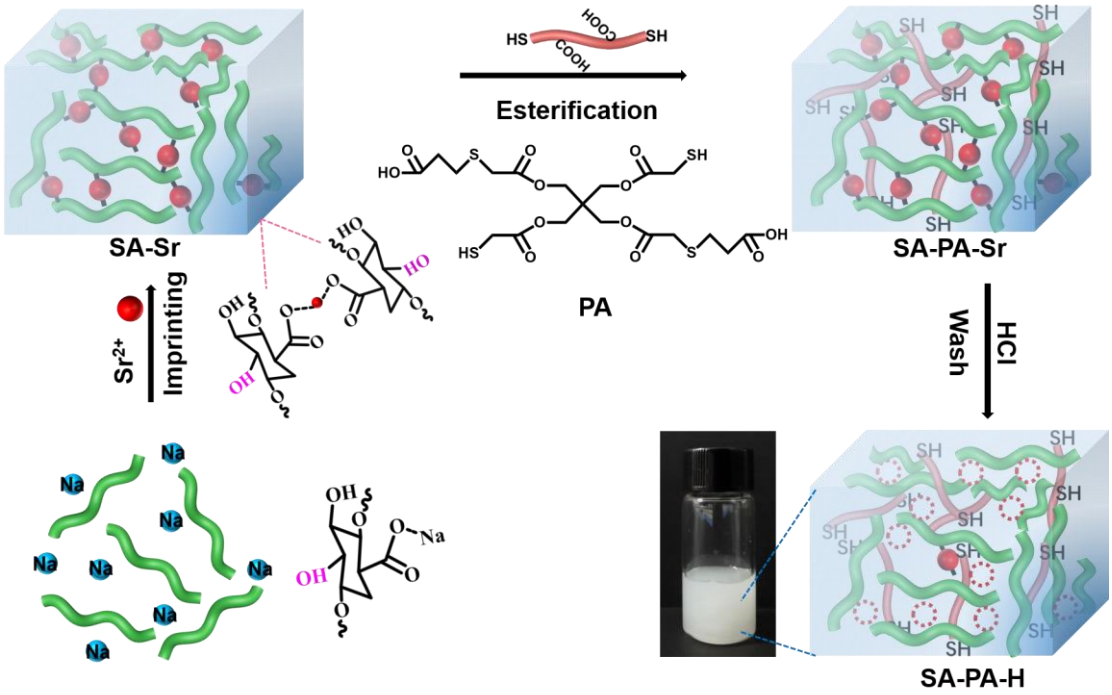

Figure 1. Synthesis route of ion-imprinted thiol-functionalized SA-PA-H composite adsorbent from SA matrix, PA crosslinker and Sr. The synthesis includes three steps: (1) The chelation between Sr^{2+} and carboxylate groups in SA to prepare SA-Sr hydrogels. (2) Acid-catalyzed esterification between hydroxyl groups in SA-Sr and carboxylic groups in PA to generate thiol-functionalized cross-linked hydrogels SA-PA-Sr. (3) Preparation of ion-imprinted SA-PA-H adsorbents by washing the SA-PA-Sr hydrogels with hydrochloride acid solutions to remove chelated Sr^{2+}. The inset image displays the appearance of SA-PA-H hydrogel suspended in pure water.

2.3 Materials characterization

2.3.1 Nuclear Magnetic Resonance (NMR). NMR spectra were acquired on a Bruker AV 400M spectrometer. $CDCl_3$ was used as the solvent with tetramethylsilane as the internal reference.

2.3.2 Fourier Transform Infrared (FT-IR). The infrared absorption spectra of samples were collected on a Nicolet IS50 Fourier transform infrared spectrometer (Thermo Scientific). KBr tablet methods were applied to samples. Every sample was scanned 32 times with a resolution of 4 cm^{-1} in the range of 400 cm^{-1} to 4000 cm^{-1} and the average infrared signal was adopted.

2.3.3 X-ray Photoelectron Spectroscopy (XPS). The sample chemical bonds were analyzed using an ESCANLAB Xi^+ XPS system with a monochromatic Al Kα X-ray source. An electron/ion gun was used to compensate for charge build-up on the sample during measurement. The XPS peaks were fitted using the CasaXPS software, and the binding energy was corrected with a reference to C 1s at 284.5 eV.

2.3.4 Field emission scanning electron microscopy (FE-SEM) and energy dispersive X-ray spectroscopy (EDX) mapping. The morphologies of the SA-Sr, SA-PA-Sr, and SA-PA-H samples were observed with a Hitachi Regulus 8100 cold FE-SEM coupling with EDX. The samples were sprayed with gold before the observation. The accelerating voltage was 5.0 kV and the current was 10 μA. The Octane Elect Plus X-ray spectrometer (EMAX, USA) in conjunction with SEM was used to analyze EDX elements mapping of the samples with a current of 10 μA and an accelerating voltage of 10.0 kV.

2.3.5 Inductively Coupled Plasma-Optical Emission Spectroscopy (ICP-OES). The concentration of Sr^{2+} was measured by ICP-OES (Singapore, PerkinElmer) at 407.771 nm as a specific emission

wavelength of Sr^{2+}. Solution samples subjected to the test were the initial Sr^{2+}solution and supernatants collected after adsorption experiments. The concentration of Sr^{2+} was diluted to 0-1 ppm and the solution was filtered with a 0.45 μm filter before the test. The quantification was done by converting the intensities of the samples according to the standard curve established.

2.4 Sr^{2+} Adsorption

2.4.1 Batch adsorption

All experiments were conducted using polypropylene vials to avoid Si contamination from the glassware and any potential Sr^{2+} adsorption onto the glassware, as previously reported.[10] The total volume of liquid used for the adsorption was 5 mL and the solid content of hydrogel adsorbents in liquid was fixed at 1 g/L throughout all the tests. $SrCl_2$ (^{87}Sr) was dissolved in deionized water to simulate radioactive wastewater polluted by $^{90}Sr^{2+}$. Solutions with Sr^{2+} concentrations varying from 10 ppm to 500 ppm were prepared by diluting a 1000 ppm Sr^{2+} stock solution. In polypropylene centrifuge tubes, suspension of hydrogel adsorbents in Sr^{2+} solution was thoroughly mixed using an orbital shaker at 200 rpm for 24 h to promote the diffusion of Sr^{2+} into the hydrogel. Then sample tubes were centrifuged at 11,000 rpm for 15 min, and the supernatant was decanted and passed through a 0.45 μm syringe filter. The concentration of Sr^{2+} in the supernatant and the initial solution was determined by ICP-OES. The concentration was calibrated using $SrCl_2$ solutions of known concentrations (0, 0.1, 0.3, 0.5, 0.8 and 1 ppm) with a correlation coefficient larger than 0.999 (Figure S1).

The amount of Sr^{2+} adsorbed by the solids, q (mg/g), was determined using the following equation:

$$q = \frac{(C_O - C_e)V}{m} \quad (1)$$

where C_o and C_e are the initial and equilibrium Sr^{2+} concentrations, respectively; V (L) is the volume of the suspension, and m (g) is the amount of the adsorbent (mass of solid fraction of the hydrogel).

Adsorption kinetics was measured at room temperature using a fixed initial Sr^{2+} concentration (C_o = 100 ppm) with a solid-to-liquid ratio of 1 g/L under neural conditions. The concentration of Sr^{2+} in the solution was measured at adsorption time varying from 10 min to 24 h. For

investigation of pH dependence, hydrogel adsorbents were tested across a pH range of 2 to 12 with C_o =100 ppm. The pH was adjusted by 1.0 M HCl or 1.0 M NaOH. All other experimental parameters followed the same procedure described above.

The selectivity of Sr^{2+} in the presence of competitive ions was investigated by suspending 1 g/L hydrogel adsorbents in solutions containing Sr^{2+} (10 ppm) with varying Na^{+} concentrations (100, 200, 400 and 800 ppm). After the samples were shaken for 24 h, the supernatant was separated and its Sr^{2+} concentration was determined by ICP-OES.

2.4.2 Desorption of Sr^{2+} and reuse of hydrogel

The regeneration of SA-PA-H hydrogel was investigated. For this, the hydrogel adsorbents were first subjected to Sr^{2+} adsorption experiment in Sr^{2+} solution (100 ppm) with a solid content of 1 g/L, orbital shaking at 200 rpm for 12 h to reach saturated adsorption. Then the saturated adsorbents were fully washed with ultrapure water and submerged in 100 mL hydrochloric acid (0.5 mol/L) with a solid-to-liquid ratio of 4 g/L for 6 h under stirring to remove the adsorbed Sr^{2+}. After washing and centrifuging, the regenerated hydrogel adsorbent was collected and added to a Sr^{2+} solution (100 ppm) again to repeat the adsorption experiment under identical conditions (i.e. solid content 1g/L, orbital shaking at 200 rpm for 12 h). After the sorption experiments and centrifugation, the concentration of Sr^{2+} in the filtered supernatant was measured by ICP-OES to determine the adsorption capability of the regenerated adsorbent. The same procedure was repeated four times to investigate the stability and reusability of the regenerated SA-PA-H hydrogel as an adsorbent.

2.4.3 Filtration test

Filtration membranes composed of SA-PA-H hydrogel were prepared by depositing the hydrogel at varying amounts (0.02-0.1 g) on a Nylon 6 filtration membrane with a pore size of 0.2 μm held by the sand core in a funnel with an inner diameter of 30 mm. Then the tunnel holding the SA-PA-H membrane was attached to a suction filter bottle connected to a vacuum pump. Then 100 mL Sr^{2+} (0.78 ppm) solution was added to the tunnel and the pump was turned on to make a vacuum. By adjusting the pressure in the suction bottle, the Sr^{2+} solution was filtrated through the

membrane driven by a pressure difference across the membrane. After the filtration was completed, the filtration time was recorded to calculate the flux. The effluents were taken from the suction bottle and Sr^{2+} concentrations were determined by ICP-OES.

2.5 Rheology test

Rheological properties of the fabricated hydrogel were measured by an HR-20 stress-controlled rheometer (TA measurement, USA) with a disposable 25 mm diameter parallel plate. The geometry gap was set to 1220 μm. A strain sweep test was first carried out at an oscillation frequency (ω) of 1 rad/s, and then frequency sweep tests were performed within a linear viscoelastic regime with a strain amplitude (γ) of 0.5%. To investigate the relaxation/recovery behavior of the hydrogel in response to an applied shear strain, the hydrogel was subjected to an oscillation shear with following strain amplitudes and durations (in parentheses) executed in sequence: 0.1% (300 s), 1000% (300 s), 0.1% (600 s), 1000% (300 s), 0.1% (600 s), 1000% (300 s), 0.1% (1200 s). The temperature was maintained at 25 °C throughout all the measurements.

3 Result and Discussion

3.1 Synthesis and characterization of thiol-functionalized Sr^{2+} imprinted SA hydrogels

3.1.1 Synthesis of thiol group-functionalized crosslinker PA

To develop an efficient adsorbent for Sr^{2+} removal with a high sorption capacity and selectivity, strategies of Sr^{2+} imprinting and introduction of as many thiol groups as possible to the adsorbent were considered in the present study based on sodium alginate (SA) hydrogel. To introduce thiol groups into a SA hydrogel, PET4A owing 4 thiol groups in one molecule was adopted as a crosslinker of SA via modification with acrylic acid (AA) to gain carboxylic groups for esterification with SA (Scheme 1). The modification was realized by a one-step thiol-ene click reaction between thiol groups of PET4A and about 2.2 equivalents of AA, with the product named PA (Scheme 1). ^1H NMR spectra of the products and the substrate mixtures dissolved in $CDCl_3$ were compared in Figure 2. In the spectrum of substrates, signals with chemical shifts at 5.95-6.65 ppm were ascribed to alkenyl protons of acrylic acids (H^d, H^f and H^e), which disappeared in the spectrum of PA products indicating a full conversion of acrylic acid. In the spectrum of PA product,

peaks ascribed to methylene protons ($H^{e'}$ and $H^{f'}$) near thioester and carboxylic groups at 2.71 ppm and 2.93 ppm respectively are observed. At the same time, the peak at 2.06 ppm ascribed to thiol groups remained but slightly weakened after the reaction. Using the integral of H^{a} ($H^{a'}$) as an internal standard, the conversion of the thiol group in PET4A was determined to be 34%. The results showed that an average of 1.8 thiol groups remained in every modifier/crosslinker PA molecule in the mixture product. The ^{1}H NMR demonstrated the successful synthesis of thiol- and carboxylic-functionalized PA, being an ideal crosslinker of SA hydrogel whilst introducing a large amount of thiol groups to improve the Sr^{2+} sorption capacity of the hydrogel.

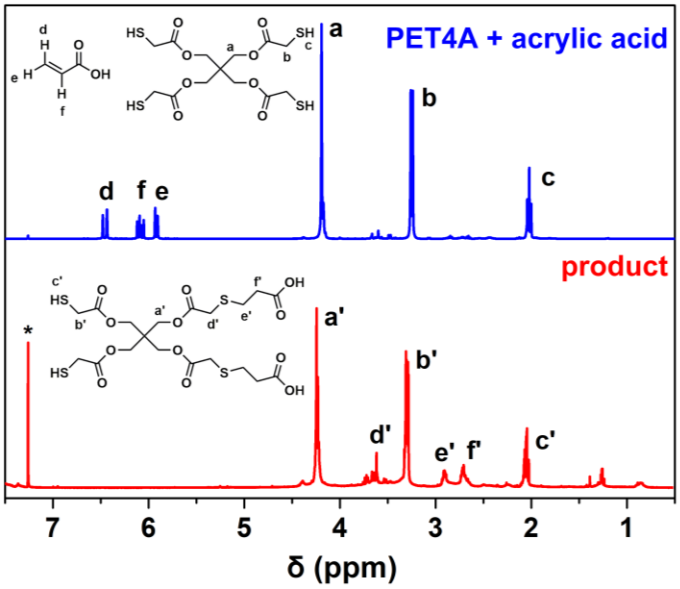

Figure 2. ^{1}H NMR spectra of PET4A mixed with 2.2 equiv. acrylic acid (up) and product PA dissolved in $CDCl_3$ (bottom, *: CH_3Cl).

The FTIR spectrum of PA was compared with the spectra of PET4A and acrylic acid as shown in Figure 3a. In contrast to the evident peak around 1650 cm^{-1} in the AA spectrum, the characteristic adsorption of C=C disappeared in the IR spectrum of PA, which further validated the full conversion of acrylic acid. The dispersive adsorption band ascribed to O-H vibration around 3200 cm^{-1} increased due to the prevalent carboxylic group and adsorbed moisture in PA. The adsorption signal at 2574 cm^{-1} revealed the presence of the thiol group which was also observed in the spectrum of PET4A. The FTIR spectra confirmed the synthesis of PA containing essential thiol groups to provide potential adsorption sites for Sr^{2+} when used to fabricate SA hydrogel adsorbent.

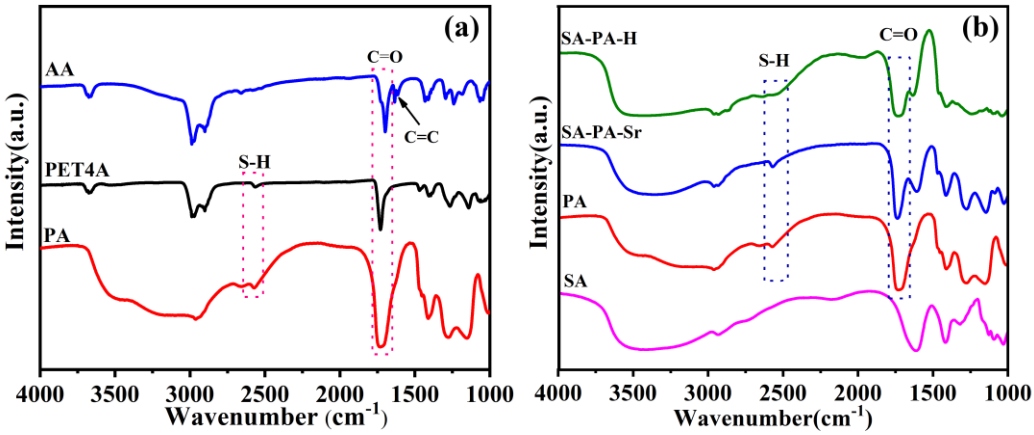

Figure 3. (a) FTIR spectra of AA, PET4A and PA. The characteristic S-H, C=O and C=C vibration adsorption peaks are highlighted by the boxes and an arrow. (b) FTIR spectra of SA, PA, SA-PA-Sr and SA-PA-H. The characteristic S-H and C=O vibration adsorption peaks are highlighted by the boxes.

3.1.2 Fabrication of the thiol-rich and Sr^{2+} imprinted hydrogel SA-PA-H

A three-step route was carried out to fabricate a thiol-rich and Sr^{2+} imprinted SA-based hydrogel adsorbent as illustrated in Figure 1. The synthesis procedure has been described in section 2.2.2 and 2.2.3 in detail. The relatively low yield (37.2%) indicates incomplete reaction between SA-Sr and PA, that is, the SA-PA-H was far from being fully crosslinked. The unreacted hydroxyls and pendant chains in the hydrogels assure good hydrophilicity and enough free volume of the adsorbents for the diffusion of water molecules and Sr^{2+} ions. FTIR was applied to examine the structures of the prepared SA-PA-Sr and SA-PA-H hydrogels (Figure 3b). In the spectrum of SA-PA-Sr, there were two carbonyl peaks at 1733 cm^{-1} and 1631 cm^{-1}. The peak at 1631 cm^{-1} was ascribed to the vibration of C=O bonds in the carboxyl group, which is confirmed by the spectrum of SA containing only carboxyl groups rather than ester groups. Meanwhile, the C=O vibration peak at 1733 cm^{-1} corresponded to ester carbonyl groups. The characteristic carbonyl absorption signal was absent in the spectrum of SA but observed in the spectrum of PA which was abundant with the ester group. The reduction of carboxyl absorption and the co-existence of the ester group and the carboxyl group suggested partial esterification of SA with PA. The unreacted carboxyl group was arguably due to the chelation of carboxyl groups with Sr^{2+}, which prevented them from esterification. The esterification between carboxylic groups and hydroxyl groups was also

supported by a slightly decreased broad O-H absorption band in the range of 3000−3500 cm^{-1} in SA-PA-Sr as compared with the spectrum of SA. On the other hand, S-H vibration signals were clearly observed in SA-PA-Sr indicating the existence of thiol groups in SA-PA-Sr. The FTIR spectrum demonstrated that SA-PA-Sr has the expected chemical structure. The partial esterification allowed SA-PA-Sr to be protonated to SA-PA-H as the intact ion-imprinted crosslinked hydrogel-bearing carboxyl group and thiol group as dual adsorption sites. In contrast, SA-Sr without covalent crosslinking would lose integrity in hydrochloric acid due to the break of Sr^{2+} chelation.

Morphologies of SA-Sr, SA-PA-Sr and SA-PA-H were investigated by SEM (Figure 4). As Figure 4a&b displayed, the SA-Sr hydrogel was a well-defined porous network composed of layered structures with smooth surfaces. The micron-sized pores were likely to be the result of water loss from swelled hydrogel during the preparation of SEM samples. SA-PA-Sr was also a three-dimensional (3D) porous network composed of platelets (Figure 4c&d). However, the surface of the platelets is rougher and more porous than SA-Sr. The difference in the morphology could be explained by the modification of hydrogel by esterification crosslinking of SA and PA, which led to slightly contracted and wrinkled surfaces. After elution with acid, the hydrogel (SA-PA-H) has a morphology consisting of collapsed agglomerates (Figure 4 e&f). This is because in the SA-Sr and SA-PA-Sr hydrogels, Sr^{2+} acted as non-covalent crosslinkers, by complexing with carboxyl groups from different SA chains, to construct the 3D network structures of the hydrogels, which were however eliminated during the acid elution. The exchange of Sr^{2+} by proton largely reduced the number of the non-covalent crosslinkers, triggering partial agglomerates of the framework platelets. In spite of this, the SA-PA-H still maintained the form of hydrogel containing a large content of water (i.e. 94.4%) as demonstrated above. The morphology alternation confirms the efficient removal of the Sr^{2+} via acid elution, forming ion-imprinted cavities in the SA-PA-H as adsorption sites.

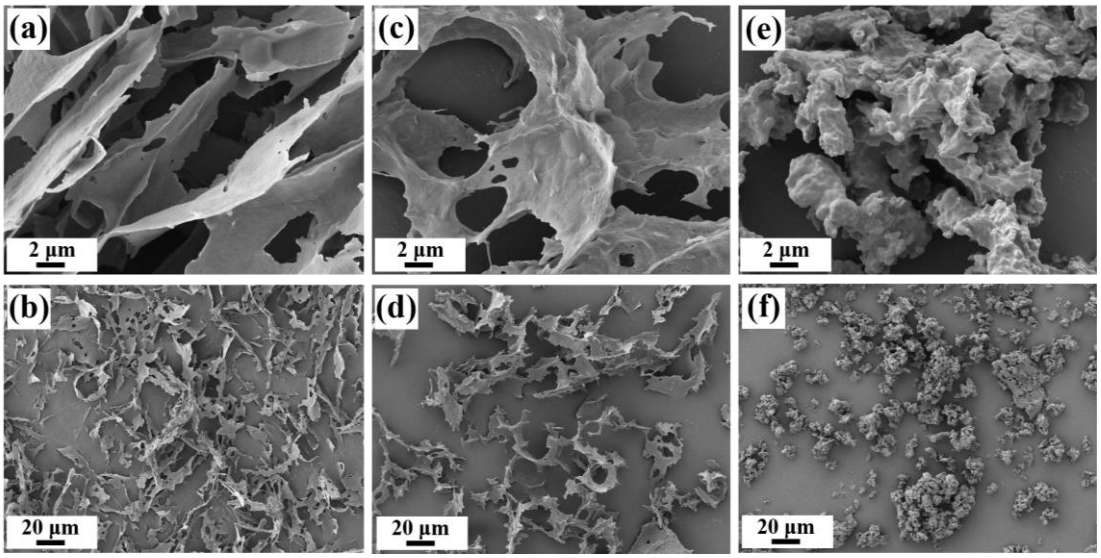

Figure. 4. SEM images of SA-Sr (a-b), SA-PA-Sr (c-d) and SA-PA-H (e-f) samples coated by gold and observed at different magnifications.

The distribution of Sr, O and S elements in SA-Sr (Figure S2), SA-PA-Sr (Figure S3) and SA-PA-H (Figure 5) hydrogels were further studied by SEM-EDX to confirm the successful synthesis of SA-PA-H composite hydrogels with Sr-imprinted moieties. In the EDX elemental map of SA-Sr (Figure S2), the intensity of S elements was barely stronger than the background noise. The observed trace amount of sulfur likely stemmed from sulfonic groups in the emulsifier AOT used during the preparation of SA-Sr hydrogel. After modification by PA, SA-PA-Sr and SA-PA-H hydrogel showed strong signals of S elements in its EDX elemental map (Figure S3&5), which indicated successful incorporation of PA along with abundant thiol groups into the hydrogels. For the Sr element, both EDX elemental maps of SA-Sr and SA-PA-Sr exhibited strong Sr signals (Figure S2&S3), implying the prevalence of Sr^{2+} adsorbed in the hydrogels. Compared with SA-Sr and SA-PA-Sr, the intensity of Sr element diminished obviously in the EDX elemental map of SA-PA-H (Figure 5). The results revealed that the majority of Sr^{2+} chelated in the hydrogel was removed by washing it with hydrochloric acid. The intensities of O elements remained almost unchanged through the preparation, suggesting backbones of the hydrogels remained stable. The EDX elemental mapping validated the successful fabrication of the thiol-rich and ion-imprinted SA-PA-H hydrogel adsorbent by the three-step protocol.

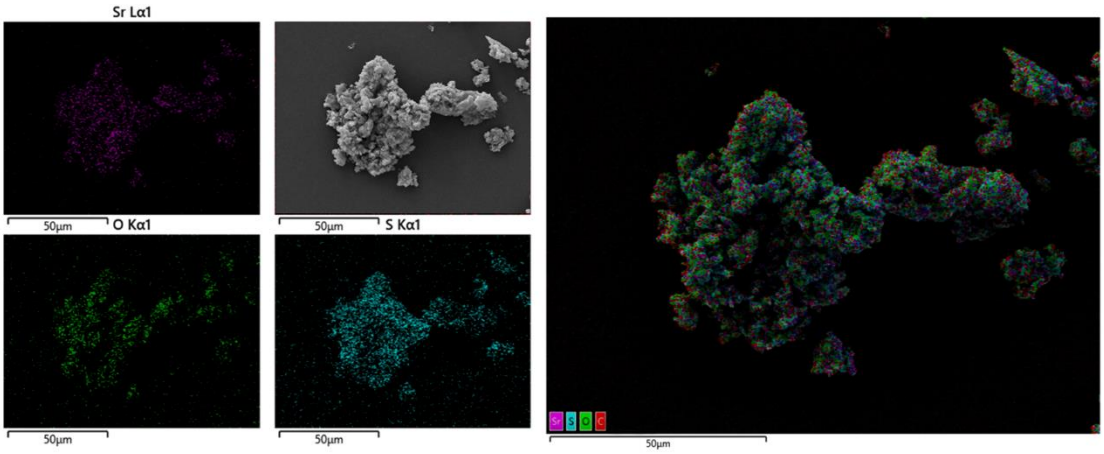

Figure. 5. EDX elemental maps along with the SEM image of SA-PA-H showing the distribution of Sr, O and S in the sample by purple, green and cyan, respectively.

To further reveal the composition and interaction between components (e.g. SA, PA and Sr^{2+}) in the composite hydrogels, XPS spectra (Figure 6) along with high-resolution S2p spectra (Figure 6b) of the hydrogels were investigated. Due to spin-orbital coupling, deconvolution of every merged S2p peak presented closely coupled peaks ascribed to $S2p_{1/2}$ and $S2p_{3/2}$ photoelectron lines (Figure 6b). In the spectrum of SA-Sr hydrogel, the peaks at 169.1 and 167.7 eV can be assigned to the sulfonate ($-SO_4^-$) group introduced by trace AOT during preparation. The existence of sulfonate peaks explained the trace sulfur signal in the EDX mapping of SA-Sr (Figure S2). After PA was added to SA-Sr followed by esterification, three deconvoluted S2p peaks with different binding energies at 168.2, 164.6 and 163.4 eV appeared in the XPS spectrum of SA-PA-Sr (Figure 6b). The peaks at 164.6 and 163.4 eV originated from thiol anion S ($-S^-$) chelating with Sr^{2+}, and the peak at 168.2 eV was attributed to protonated thiol group S (-SH) without Sr^{2+} bonded, which overlapped with sulfonate peaks and was too weak to be deconvoluted to $S2p_{1/2}$ and $S3p_{3/2}$ peaks. The three characteristic peaks were also observed in the XPS spectrum of SA-PA-H (Figure 6b). However, the ratio between the integral area of the $-S^-$ peaks over the area of the -SH peak decreased in SA-PA-H as compared to SA-PA-Sr, which indicated the dissociation of Sr^{2+} from sulfur and an increased amount of protonated sulfhydryl group. The results demonstrated that PA successfully modified the SA hydrogel and introduces sulfur sites for Sr^{2+} binding. By washing with acid, the Sr^{2+} was partially removed from SA-PA-Sr and the sulfhydryl group was recovered in SA-PA-H to serve as potential Sr^{2+} adsorption moieties.

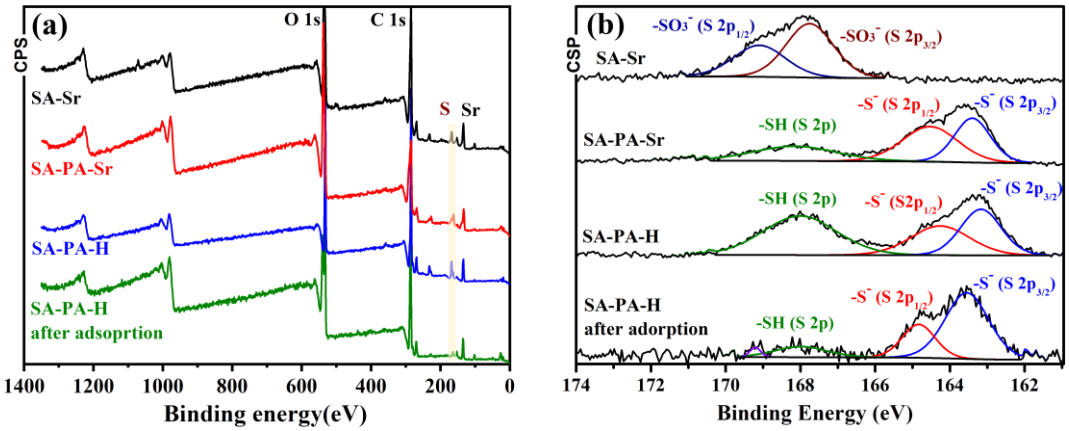

Figure 6. (a) XPS survey spectra of SA-Sr, SA-PA-Sr, SA-PA-H and SA-PA-H after adsorption of Sr^{2+}. The signals of electrons in O 1s, C 1s and Sr are labeled close to the corresponding peaks, and the electron signal of S is highlighted by the yellow box. (b) High resolution XPS spectra of S 2p peaks of SA-Sr, SA-PA-Sr, SA-PA-H and SA-PA-H after adsorption of Sr^{2+}. The S 2p peaks are deconvoluted to separated peaks labeled with corresponding sulfur-containing groups.

3.2 Hydrogel rheology

The viscoelasticity of the SA-PA-H hydrogel was investigated for its further application as membrane materials. The swollen hydrogel was subjected to a strain sweep test and a frequency sweep test at room temperature (T = 25 °C). The results are shown in Figure 7a&b. It is found that the SA-PA-H is elastic as storage modulus (G') > loss modulus (G'') at small strain, while yield beyond a critical strain where γ = 4.4% and G' = G''. The frequency sweep confirmed that the SA-PA-H is strongly elastic with G' ≈ 10 kPa, and G' is larger than G'' throughout all shear frequencies. The elasticity is ascribed to the network structure of SA-PA-H crosslinked by esterification. Moreover, there would be massive hydrogen bonding formed between ester, carboxyl, hydroxyl and thiol groups, which can further strengthen the hydrogel.

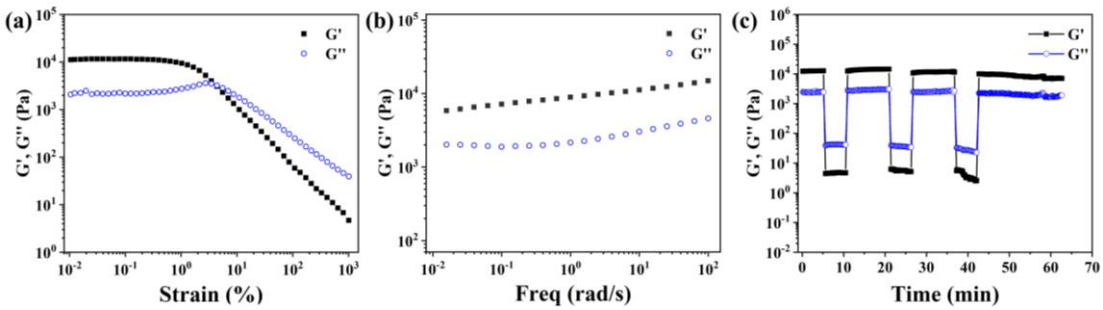

Figure 7. (a) G’ and G’’ of SA-PA-H hydrogel in strain sweep test under oscillation shear at 1 rad/s frequency. (b) Frequency-dependent G’ and G’’ of SA-PA-H under oscillation shear at a strain amplitude of 0.5%. (c) Step-strain behavior of SA-PA-H indicating a reversible recovery in G’ and G’’ at small strain (0.1%) after yielding at large strain (1000%).

A step-strain experiment was performed to demonstrate the self-recovery ability and the processability of the SA-PA-H hydrogel (Figure 7c), which was expected to be realized by reversible dissociation and reformation of non-covalent hydrogen bonds in the hydrogels. The swollen hydrogel was subjected to an oscillation shear by small strains (0.1%) and large strains (1000%) alternately and the result is shown in Figure 7c. Initially, the hydrogel was sheared at a small strain below the yield point, where γ = 0.1% at ω= 1.0 rad/s. The G’ and G’’ of the SA-PA-H are about 13 kPa and 2.4 kPa, respectively, indicating that the hydrogel is in a quasi-solid state. As the strain increased to 1000% beyond the yield point, G’ and G’’ significantly decreased to ~4.4 Pa and ~40 Pa (i.e. tan $\delta \equiv$G’’/G’~8.8-9.3), respectively (Figure 7c), indicating the hydrogel was in a liquid state. Nevertheless, when the strain was decreased to 0.1%, the G’ recovered to 13 kPa immediately and tan δ of the hydrogel decreased to 0.21 at the same time, revealing that the hydrogel recovered to a quasi-solid state. In the subsequent strain-step alternations, repeated yielding and recovery of the hydrogel were observed, demonstrating no significant loss in the viscoelasticity nor a change in the rate of structural reformation of the hydrogel even underwent repeated large strain deformations. Only a small drop of G’ and G’’ was observed in the last strain-step test (4^{th} cycle) due to the loss of water from the hydrogel after long-time measurement (Figure 7c). The behavior demonstrated that SA-PA-H hydrogel can be readily processed and reshaped without damaging its mechanical properties thanks to the presence of massive hydrogen bonds between polymer chains. The robustness with strong elasticity allows us to reshape the fabricated hydrogel into membrane filtration devices for facile water purification, which will be discussed in section 3.3.5.

3.3 Strontium adsorption

3.3.1 Isothermal adsorption

To investigate the ability of the hydrogels to remove radioactive Sr^{2+} from polluted water, we examined the isothermal adsorption behavior of SA-PA-H and SA-Sr in simulated Sr^{2+} solutions. The well-known Langmuir model was applied to describe Sr^{2+} adsorption behaviors, assuming: (i) surface monolayer sorption, (ii) a finite number of binding sites, (iii) uniform sorption energies, and (iv) no transmigration of sorbates in the plane of the surface. Adsorption (q, mg of adsorbate/g of adsorbent) of Sr^{2+} by the hydrogels was plotted against equilibrium Sr^{2+} concentration (C_e, ppm) in solution as shown in Figure 8a. The adsorption data were fitted by the Langmuir isotherm:

$$q = \frac{bq_m C_e}{1+bC_e} \quad (2)$$

where b is the Langmuir constant related to the affinity coefficient of binding sites (L/mg) and q_m is the maximum sorption capacity of Sr^{2+} for the adsorbent.

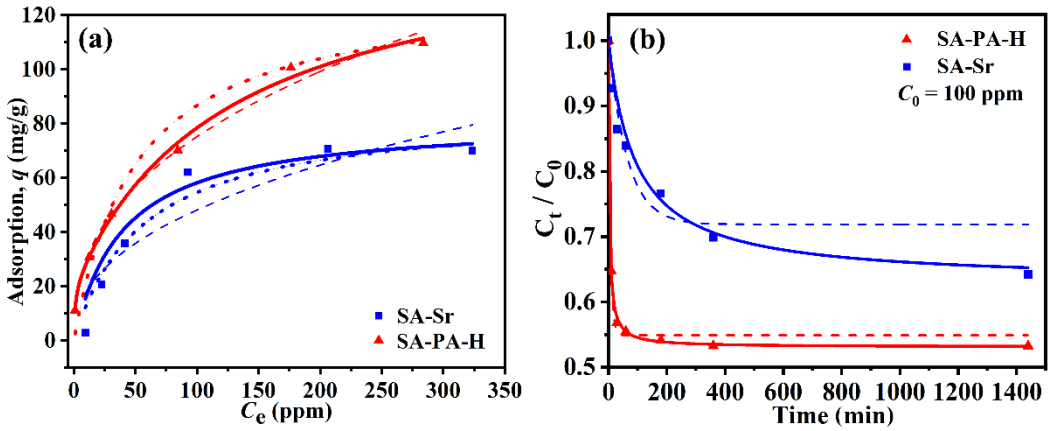

Figure 8. (a) Sr^{2+} adsorption isotherm with adsorption (q) plotted against the equilibrium concentration (C_e) for SA-PA-H and SA-Sr. The dotted, solid and dashed lines are fittings according to single-site Langmuir, dual-site Langmuir and Freundlich isotherm models, respectively; (b) Sr^{2+} adsorption kinetics by SA-PA-H and SA-Sr at C_0 = 100 ppm. The dashed and solid lines are fittings according to PFORE and PSORE, respectively.

As shown in Figure 8a, the adsorption data of both SA-PA-H and SA-Sr can be fitted by single-site Langmuir isotherm with a decent correlation coefficient (dotted lines, R^2 = 0.961 and 0.971, respectively). Table 1 lists the Langmuir fitting parameters, q_m and b of the hydrogels. As can be seen, the SA-PA-H had an excellent adsorption capacity with a high q_m value of 130.0 mg/g. In contrast, the q_m of SA-Sr is much lower (87.9 mg/g) due to that a majority of the sorption sites (e.g. the carboxyl groups in SA) were already occupied by Sr^{2+}. The adsorption results indicated

488 the importance of the Sr^{2+}-imprinted cavities obtained via acid elution of the SA-PA-Sr to remove
489 pre-complexed Sr^{2+} and of the thiol groups introduced by PA in enhancing the Sr^{2+} adsorption
490 capacity of the SA-PA-H hydrogel.

491

492 Table 1. Single-site, dual-site Langmuir and Freundlich isotherm models for Sr^{2+}adsorption

Sample	Langmuir model			dual-site Langmuir model					Freundlich model		
	q_m (mg/g)	b (L/mg)	R^2	q_{m1} (mg/g)	b_1 (L/mg)	q_{m2} (mg/g)	b_2 (L/mg)	R^2	K_F (mg^{1-n} $\bullet L^n/g$)	n	R^2
SA-PA-H	130.0	0.02	0.961	20.5	0.98	131.2	0.007	0.991	11.92	0.400	0.989
SA-Sr	87.9	0.01	0.971	25.7	0.01	62.2	0.011	0.939	6.750	0.427	0.813

493

494 Considering that in the SA-PA-Sr hydrogel both the ion-imprinted cavities located at the
495 carboxyl groups in SA chains and the thiol groups introduced from PA would contribute to the Sr^{2+}
496 adsorption as different sorption sites with different sorption energies, the dual-site Langmuir
497 adsorption model was also used to fit the adsorption data:

498 $$q = \frac{b_1 q_{m1} C_e}{1+b_1 C_e} + \frac{b_2 q_{m2} C_e}{1+b_2 C_e} \quad (3)$$

499 where the fitting parameters b_1 and b_2, and q_{m1} and q_{m2} represent the affinity coefficients (L/mg)
500 and the maximum sorption capacity (mg/g) for the two types of sorption sites, respectively.

501 As shown in Figure 8a (the solid lines) and Table 1, the Dual-site Langmuir model better
502 described the adsorption behavior of the SA-PA-H with a higher R^2 (0.991) than the single-site
503 Langmuir model (0.961). On the other hand, the adsorption data of SA-Sr was poorly fitted by the
504 dual-site Langmuir model (R^2 = 0.939), suggesting that the SA-Sr was a single-site adsorbent
505 (Figure 8a). The fitting results validated the two sorption sites for Sr^{2+} in the SA-PA-H hydrogel,
506 that is, the thiol group and the ion-imprinted carboxyl group, with a total maximum adsorption
507 capacity (q_m) of 151.7 mg/g. This well meets the purpose of designing the SA-PA-H using ion-
508 imprinting and thiol-rich strategies to enhance the Sr^{2+} adsorption performance. The role of the
509 thiol group was also confirmed by the XPS measurement of the SA-PA-H hydrogel after the
510 adsorption experiment. The peak ascribed to the thiol group (-SH) diminished while the peaks of
511 thiol anion ($-S^-$) were amplified when compared to the signal before adsorption (Figure 6b),
512 confirming the adsorption of Sr^{2+} to the thiol group by forming $S^-(1/2Sr^{2+})$ complex.

The adsorption data are also fitted to the Freundlich isotherm:

$$q = K_F c_e^n \quad (4)$$

where K_F is the Freundlich sorption coefficient and n is the adsorption intensity [52].

As shown in Figure 8a (dashed lines), the Fredulich isotherm successfully captures the adsorption behaviors of SA-PA-H (R^2 = 0.989, Table 1) while it fails to fit the adsorption data of SA-Sr (R^2 = 0.813). The Freundlich isotherm describes multilayer adsorption and assumes exponential decay in the energy distribution of heterogeneous adsorbed sites [52]. The excellent fitting of the Freundlich isotherm to SA-PA-H adsorption data but not the SA-Sr confirms the exsitence of more than one type of adsorption sites in SA-PA-H, that is, the carboxylic and thiol groups. This is consistent with the dual-site Langmuir model, and the values of n are lower than 1, indicating a nonlinear sorption on the adsorbents.

Moreover, to confirm the essential role of PA in the fabrication of highly efficient adsorbent, a control sample of Sr^{2+}-imprinted SA hydrogel without PA component, named SA-H, was prepared by eluting SA-Sr with hydrochloride acid, and its Sr^{2+} adsorption performance was evaluated, with data shown in Figure S4. Since the data failed to be fitted by Langmuir models (see discussion in the Supporting Information), the comparison of adsorption performance between SA-H and SA-PA-H, SA-Sr was done at given C_es. The general trend clearly showed a worse adsorption capability of the SA-H than SA-PA-H. For example, at C_e = 250 ppm, the q of SA-H was only 48 mg/g, while q of SA-PA-H was ~ 103.9 mg/g. Surprisingly, at a given C_e, the q of SA-H was even smaller than that of SA-Sr whose carboxyl groups had been chelated with Sr^{2+}. One possible reason was that during the acid elution, progressive esterification between carboxyl groups and hydroxyl groups in SA would occur as catalyzed by acid, which can significantly abolish the adsorption sites of carboxyl groups. In contrast, in the presence of PA, hydroxyl groups in SA had been consumed by esterification with carboxyl groups from PA. Thus, the carboxyl groups of SA were kept intact and imprinted by Sr^{2+} during the acid elution process, potentially acting as selective adsorption sites for Sr^{2+}. This indicates that PA is an indispensable modifier for SA to achieve the successful preparation of efficient Sr^{2+}-imprinted adsorbents.

3.3.2 Adsorption kinetics

Sr^{2+} adsorption kinetics of SA-PA-H and SA-Sr were studied. As shown in Figure 8b, SA-PA-H adsorbed Sr^{2+} in a very fast manner, with the adsorption equilibrium almost reached in 30 min. In contrast, Sr^{2+} adsorption of SA-Sr was relatively slow, having the adsorption equilibrium even not fully reached in the experiment time (12 h). To quantify the adsorption kinetics of the hydrogels, the data were fitted by a pseudo-first order rate equation (PFORE) and a pseudo-second order rate equation (PSORE):

$$\log(q_e - q_t) = \log(q_e) - \frac{k_1}{2.303}t \quad (5)$$

$$\frac{t}{q_t} = \frac{1}{k_2 q_e^2} + \frac{t}{q_e} \quad (6)$$

where q_t and q_e are adsorbed Sr^{2+} quantities (mg/g) at time t and equilibrium respectively, and k_1 and k_2 are a first order and a second order rate constant, respectively.

The fitting parameters are shown in Table 2. The PSORE fitted the adsorption kinetics of SA-PA-H very well with $R^2 > 0.99$, while the PFORE failed to describe the adsorption kinetics of both the SA-PA-H and the SA-Sr hydrogels. The possible reason for the preference to the PSORE kinetics instead of PFORE kinetics is that the adsorption of a single Sr^{2+} is a second order reaction involving physicochemical interactions between two phases, that is, a Sr^{2+} cation from solution and a binding group, i.e. carboxylic or thiol group, from solid phase. In the fitting results based on PSORE, significantly higher k_2 (0.67 g mg^{-1} min^{-1}) and q_e (46.9 mg g^{-1}) of SA-PA-H than SA-Sr indicated an excellent adsorption activity of the SA-PA-H. The enhanced adsorption kinetics of the SA-PA-H were attributed to the multiple sorption sites and the likely promotion by Sr^{2+}-imprinting and the additional adsorption sites of thiol groups.

Table 2 Fitting parameters of PFORE and PSORE for Sr^{2+} sorption by SA-PA-H and SA-Sr

Sample	PSORE			PFORE		
	k_2 (g mg^{-1} min^{-1})	q_e (mg g^{-1})	R^2	k_2 (g mg^{-1} min^{-1})	q_e (mg g^{-1})	R^2
SA-PA-H	0.67	46.9	0.99	0.15	45.1	0.86
SA-Sr	0.03	37.0	0.91	0.02	28.1	0.69

3.3.3 pH and temperature effect

Polluted water from different resources might have various pH values and the temperature of the polluted water can also vary depending on the environment. Therefore, it is crucial to study the stability of the composite hydrogel when used to uptake Sr^{2+} in environments of different pH and temperatures to better guide its practical application in recovering Sr^{2+} from real wastewater.

For pH effect, adsorption experiments were carried out at C_o =100 ppm in a pH range from 2 to 12 (Figure 9a). The adsorption behavior of SA-PA-H for Sr^{2+} are evaluated by the adsorption capacity and removal efficiency (*E*). The filtration efficiency is evaluated by removal efficiency (*E*) calculated from equation (7):

$$E(\%) = \frac{C_o - C_e}{C_0} \times 100\% \quad (67)$$

where C_o and C_e are initial and equilibrium concentrations of Sr^{2+} measured by ICP-OES.

Over a wide range of pH (4-10), the sorption capacity of SA-PA-H towards Sr^{2+} was almost unchanged with a q ~ 41 mg/g and a removal efficiency around 54%-57%. The SA-PA-H showed superior stability in solutions with various pH. However, when the solution pH was lowered to 2, the sorption capacity q dropped to 17.7 mg/g, only ~ 40% of that of the other pH values. The suppressed adsorption here was owing to the high concentration of H^+ competing with Sr^{2+} to bind with carboxyl groups. On the other hand, when suspended in a more basic Sr^{2+} solution with pH of 12, the swollen SA-PA-Hs were observed to degrade into water soluble substances with the suspension becoming a clear solution. This is likely due to that the base environment catalyzed the hydrolysis of ester crosslinks in SA-PA-H, resulting in the degradation of the SA-PA-H into water soluble anionic SA and PA. Therefore, the adsorption of SA-PA-H at more alkaline pH cannot be evaluated, while the experiment demonstrated a possible way of degradation of the adsorbents after use.

To further elucidate the effect of H^+ on SA-PA-H hydrogel, the Zeta potential of the hydrogel was measured (Figure 7b). When the pH value was greater or equal to 4, the majority of carboxyl groups in SA-PA-H were deprotonated and existed as carboxy anions, which negatively charged the surface of the hydrogel with a low Zeta potential around -40.0 mV. As the pH was decreased to 2, the carboxyl groups in the hydrogel were protonated, resulting in an increase of the Zeta potential to -14.6 mV. The different states of the carboxyl groups revealed by the Zeta potential measurement demonstrated the important role of carboxy anion as available sites for Sr^{2+} sorption,

596 which could be modulated by pH to realize Sr^{2+} desorption and regeneration of the SA-PA-H
597 adsorbent.
598

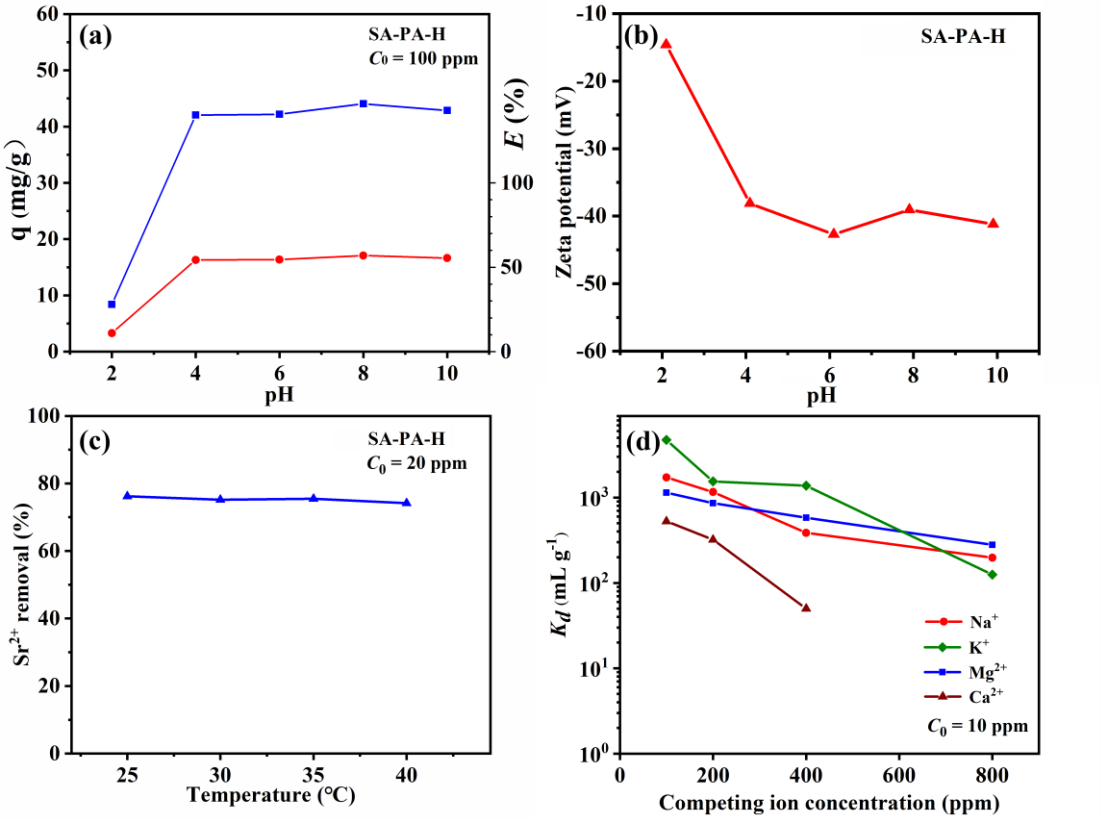

599

600 Figure 9. The effect of pH, temperature and competing ions on SA-PA-H and its adsorption. (a)
601 Sr^{2+} sorption capacity (q) and Sr^{2+}removal efficiency at C_o = 100 ppm versus pH from 2-10; (b)
602 pH dependence of the Zeta potential of SA-PA-H versus pH from 2-10; (c) Sr^{2+} removal efficiency
603 at C_o = 20 ppm versus temperature from 25°C to 40 °C; (d) Distribution coefficient K_d of Sr^{2+} (C_o
604 = 10 ppm) in brine solutions containing Na^+, K^+, Ca^{2+} or Mg^{2+} for SA-PA-H plotted versus
605 concentration of the competing ions ranging from 200 ppm to 800 ppm. The adsorption of Sr^{2+} in
606 the presence of 800 ppm Ca^{2+} was undetected.
607
608 Temperature effect on the adsorption performance of SA-PA-H hydrogel was further studied
609 by testing Sr^{2+} adsorption behaviors of the SA-PA-H at temperatures from 25 °C to 40 °C (Figure
610 9c) in Sr^{2+} solutions with an initial concentration C_o = 20 ppm. As shown, for the measured
611 temperatures, the removal rate of Sr^{2+} by SA-PA-H remained consistent, more than 75%, almost
612 independent of the temperature. That is, the SA-PA-H hydrogel exhibited good temperature

stability within the range of 25-40 °C. Based on adsorption data at different temperatures, the thermodynamics parameters like Gibbs free energy (ΔG^0), enthalpy (ΔH^0) and entropy (ΔS^0) of the adsorption can be calculated from the following equations (8-10)[53]:

$$K_a = \frac{q_e}{C_e} \tag{8}$$

$$lnK_a = \frac{\Delta S^0}{R} - \frac{\Delta H^0}{RT} \tag{9}$$

$$\Delta G^0 = \Delta H^0 - T\Delta S^0 \tag{10}$$

where K_a is the distribution coefficient, which equals to the ratio between adsorption (q) and equilibrium concentration of the solutes in the solution. R is the gas constant. By plotting $\ln K_a$ against 1/T, the temperature-dependent adsorption data can be fitted by the *Van't Hoff* equation (Figure S5). The ΔH^0 and ΔS^0 are calculated to be -27.1 kJ/mol and -83.2 J/(mol·K), respectively. The thermodynamics parameters obtained are listed in Table S2.

As seen in the results (Table S2), the negative ΔH^0 indicates that the adsorption of Sr^{2+} by SA-PA-H is exothermic, supported by the Sr^{2+} adsorption decline with increased temperature. On the other hand, the negative ΔS^0 shows an entropy reduction during the adsorption of Sr^{2+} by SA-PA-H, which can be a result of the configuration loss of carboxylic groups and thiol groups after binding with divalent ion Sr^{2+}. The negative ΔG^0 confirms that the adsorption occurs spontaneously under the tested conditions.

In summary, the adsorption of Sr^{2+} on SA-PA-H adsorbent is a spontaneous and endothermic process, even being efficient in complicated environments with various temperatures and pH.

3.3.4 Adsorption Mechanism

In sum of the isothermal adsorption, adsorption kinetics and thermodynamics studies, an adsorption mechanism is proposed. In the suspension of SA-PA-H, the SA-PA-H hydrogel is swollen by the water molecules with its functional groups hydrated in the medium (Figure 10a). The Sr^{2+} dissolved in the solution exchanges with protons from adsorption-active groups, *i.e.*, carboxylic and thiol groups within the ion-imprinted hydrogel. The generated Lewis bases, carboxylate and thiolate groups, serve as anionic ligands to fix Sr^{2+} in the ion-imprinted cavities whereby a single Sr^{2+} is chelated with two adsorbate groups, which could be two carboxylate

ligands, two thiolate ligands or a carboxylate ligand along with a thiolate ligand (Figure 10b). The binding of Sr^{2+} by the thiols to form thiolate species can be demonstrated by the XPS spectrum of SA-PA-H after adsorption (Figure 6b), where the -SH signals significantly diminished while an enhanced $-S^-$ signal is observed compared to those in the SA-PA-H spectrum. Since the hydrogel is demonstrated to be homogeneous with carboxylic and thiol groups distributed evenly within the hydrogel by the EDX maps (Figure 5) and the hydrogel exhibits multilayer adsorption behavior according to the fitting by the Freundlich model, it is arguably that the Sr^{2+} can be adsorbed by all the active adsorption groups throughout the fully swollen porous hydrogel, where the diffusion of Sr^{2+} is less hindered.

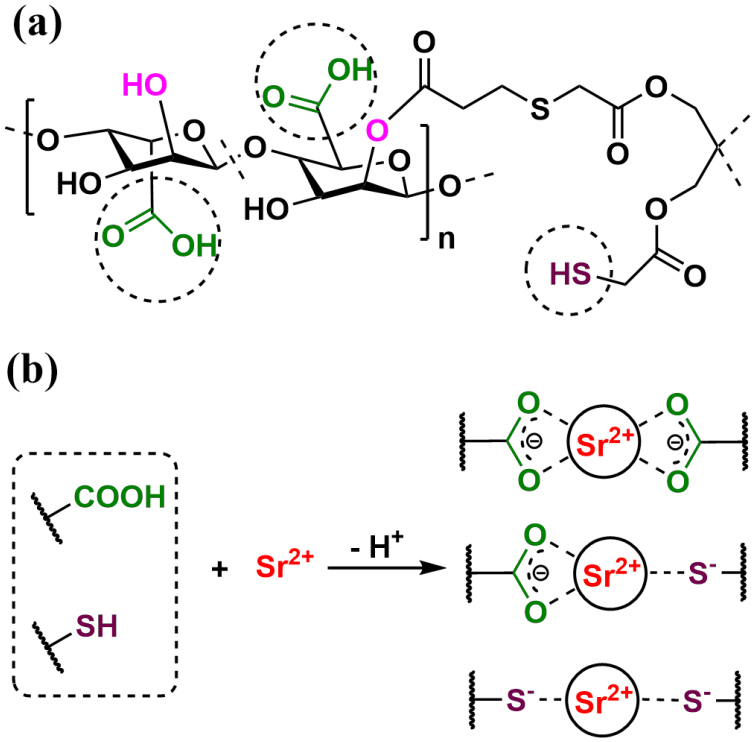

Figure 10. (a) The chemical structure of SA-PA-H (PA-crosslinked alginic acid) with adsorption-active carboxylic and thiol groups circled. (b) Ion exchange reaction between Sr^{2+} and protons in carboxylic and thiol groups. A single Sr^{2+} is bound by two carboxylate ligands, two thiolate ligands or a carboxylate ligand and a thiolate ligand.

3.3. 5 Competing ion effect

Sodium (Na^+), potassium (K^+), calcium (Ca^{2+}) and magnesium (Mg^{2+}) are the most common competing ions for Sr^{2+} when adsorbents were used in real polluted water. To figure out the

adsorption selectivity of SA-PA-H towards Sr^{2+}, the hydrogel was dispersed in Sr^{2+} solutions (C_0 = 10 ppm) containing Na^+, K^+, Ca^{2+} or Mg^{2+} with varied ion concentrations from 100 to 800 ppm. Sr^{2+} selectivity was evaluated by the distribution coefficient, K_d:

$$K_d = \frac{C_o - C_e}{C_e}\frac{V}{m} \quad (11)$$

where C_0 and C_e are the initial and equilibrium concentrations of Sr^{2+}, V is the volume (mL) of the solution, and m is the mass (g) of the absorbent.

The Sr^{2+} selectivity K_d was plotted against competing ion concentrations (Figure 9d). When the initial Na^+ concentration was 100 ppm, K_d of SA-PA-H to Sr^{2+} was as high as 1.72×10^3 mL g^{-1}. Although the K_d of SA-PA-H gradually decreased as the concentration of Na^+ was increased, SA-PA-H still showed a good adsorption selectivity towards Sr^{2+} with a K_d of 1.97×10^2 mL g^{-1} when the Na^+ concentration reached 800 ppm (Figure 9d). The good selectivity to Sr^{2+} was also observed in the presence of K^+ with K_d decreasing from 4.27×10^3 mL/g to 1.25×10^2 mL/g as the concentration of K^+ increased from 100 to 800 ppm. Similarly, when the initial Mg^{2+} concentration was 100 ppm, the K_d towards Sr^{2+} was 1.14×10^3 mL g^{-1}, which decreased to 2.80×10^2 mL g^{-1} as the Mg^{2+} concentration reached 800 ppm (Figure 9d). On the other hand, SA-PA-H selectively adsorbs Sr^{2+} at low concentrations of Ca^{2+} (100-400 ppm) with K_ds from 5.27×10^2 mL/g to 50 mL/g. However, when the Ca^{2+} is as high as 800 ppm, the adsorption of Sr^{2+} by SA-PA-H is minor. Since there is a few Sr^{2+} remaining in SA-PA-H after acid wash, the remained Sr^{2+} may exchange with Ca^{2+} who is in overwhelming excess in the competing adsorption test. Thus, the adsorption of Sr^{2+} in the presence of high concentrations (e.g. 800 ppm) of Ca^{2+} was suppressed, which may be resolved by washing the SA-PA-H hydrogel with acids for more times. All in all, the experiments demonstrated the decent selectivity of SA-PA-H to Sr^{2+} over most competing ions (Na^+, K^+ and Mg^{2+}) except Ca^{2+} at high concentrations. The selectivity was attributed to the thiol group and the ion-imprinting involved in the hydrogel. According to the hard and soft acids and bases (HSAB) principle[45], both strontium and sulfur are 'soft' atoms with thick electronic cloud be easy to deform because of their large atomic numbers. Thus, the thiol group was prone to bind with Sr^{2+} instead of Na^+, K^+ and Mg^{2+} which are regarded as 'hard' cations. Meanwhile, ion-imprinting created cavities with specific shapes and ligand distribution adapted to the geometry and charge distribution of Sr^{2+}, acting as ion sieves for Sr^{2+}. Since Sr, Ca and Mg are alkaline-earth metal

elements with the same bivalent charge when presented as cations, the volume of ion-imprinted cavities was expected to play an essential role in selectively recovering Sr^{2+} from concentrated Mg^{2+} solutions or diluted Ca^{2+} solutions in light of the size exclusion effect of the cavities. The two factors contributed together to the good selectivity of SA-PA-H towards Sr^{2+}.

3.3.6 Membrane filtration

Membrane filtration is an advanced technique for desalination and water purification with several advantages such as low cost, facile operation and ready portability.[54-56] The rheological study in section 3.2 has demonstrated that the SA-PA-H hydrogel was recoverable after large deformation, which enables SA-PA-H to accommodate certain shapes for device filtrations. A simple vacuum membrane filtration device was established by depositing swollen SA-PA-H hydrogels onto the sand core in a suction funnel equipped with a suction bottle (Figure 10a). The adsorption efficiency of the SA-PA-H membrane was investigated under vacuum filtration conditions, where 100 mL Sr^{2+} solution with a C_0 of 1 ppm passed through the membrane driven by vacuum.

After the filtration, a trace amount of Sr^{2+} was detected in the effluent in all the conditions (Figure S6), and the ion was removed completely after filtration by SA-PA-H membrane in all the conditions with extremely high removal efficiency (> 99.2%) (Figure 10b&c), which revealed the excellent adsorption efficiency of SA-PA-H in fast water purification. Varying the mass of SA-PA-H fabricating the membrane did not affect the removal efficiency of the membrane, and a complete removal (> 99.99%) of Sr^{2+} was achieved with only 0.025 g SA-PA-H (Figure 10b). An increased mass of SA-PA-H to 0.1 g decreased the water flux from 36.0 L m^{-2} h^{-1} to 6.6 L m^{-2} h^{-1} because of augmented resistance due to the thicker membrane. When the trans-membrane pressure was raised from 0.025 MPa to 0.1 MPa (Figure 10c), the flux increased accordingly from 9.6 L m^{-2} h^{-1} to 16.4 L m^{-2} h^{-1} while the removal efficiency remained unimpaired (> 99.2%). The flux can be readily regulated to produce pure water at desired rates without risks of unexpected percolation of solutes. The excellent membrane filtration performance is undoubtedly ascribed to the large adsorption capacity and the fast adsorption equilibrium of the SA-PA-H. Moreover, after the filtration the SA-PA-H membrane can be recovered from the suction funnel entirely and after

drying in the air it maintained as a free-standing membrane that can be bent elastically (Figure 10a). The good mechanical property in the dry state grants SA-PA-H great potential in fabricating portable and disposable membranes for transportation and large-scale application.

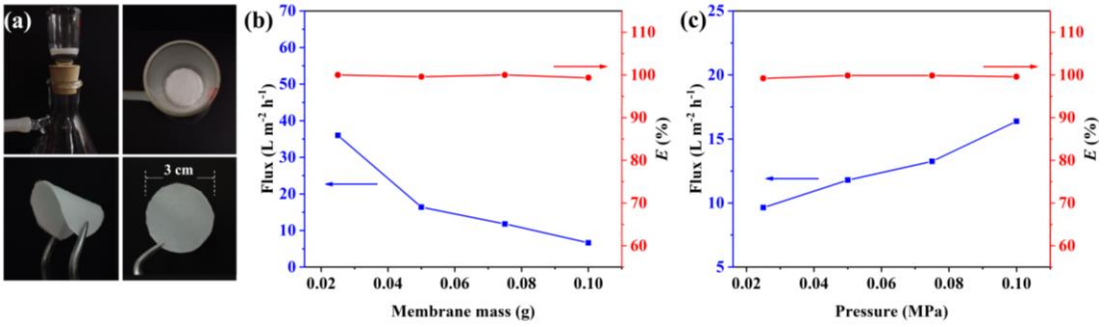

Figure 11. (a) Device consisted of a filtration funnel for vacuum membrane filtration and external appearance of a dried SA-PA-H membrane fabricated in its plat and bent forms. (b) Variation of solution flux (square, left axis) and removal efficiency (circle, right axis) as a function of membrane mass ranging from 0.02 to 0.1 g in membrane filtration experiments. (c) Variation of solution flux (square, left axis) and removal efficiency (circle, right axis) as a function of trans-membrane pressure ranging from 0.02 to 0.1 MPa in membrane filtration experiments.

3.3.7 Recyclability

Adsorption and desorption of Sr^{2+} are essential to the service life of adsorbents. An economical and environment friendly adsorbent is expected to have good recyclability and stability. To assess the recyclability and stability of the SA-PA-H adsorbent, Sr^{2+} was removed from the saturated adsorbent by hydrochloric acid to recover sorption sites after one batch adsorption experiment. Then the regenerated adsorbent was subject to a new adsorption experiment with the same initial Sr^{2+} concentration (C_0 = 100 ppm). In every adsorption cycle, adsorption efficiency (E) was calculated by equation (7).

As Figure 11 shows, the E of freshly-prepared SA-PA-H was 53.51% and the adsorption capacity (q) was 51.8 mg/g. In the first, second, third and fourth desorption-adsorption cycle, E of regenerated adsorbents dropped slightly to 47.83%, 46.28%, 36.88% and 35.22%, respectively. The attenuation of adsorption efficiency was only about 10%-20% in every regeneration taking the hydrogel in the last cycle as the reference, indicating decent stability of the hydrogel. Since there was an unavoidable loss of SA-PA-H hydrogel content during the recycling involving

centrifugation, the actual recycle efficiency was expected to be higher than the experimental values. The loss of adsorption capacity may also be attributed to the deterioration of adsorption sites resulting from the acid-catalyzed esterification between hydroxyl and carboxylic groups during acid wash in the regeneration step. The results showed that through washing with acids SA-PA-H adsorbent could be regenerated conveniently. In the meantime, protonation of the hydrogels released the adsorbed Sr^{2+} into the acid solutions, which enables an efficient separation of Sr^{2+} from the contaminated water. The robustness allowed SA-PA-H to serve as a recyclable and environment friendly adsorbent to recover Sr^{2+} from polluted water with little waste and reagent contamination.

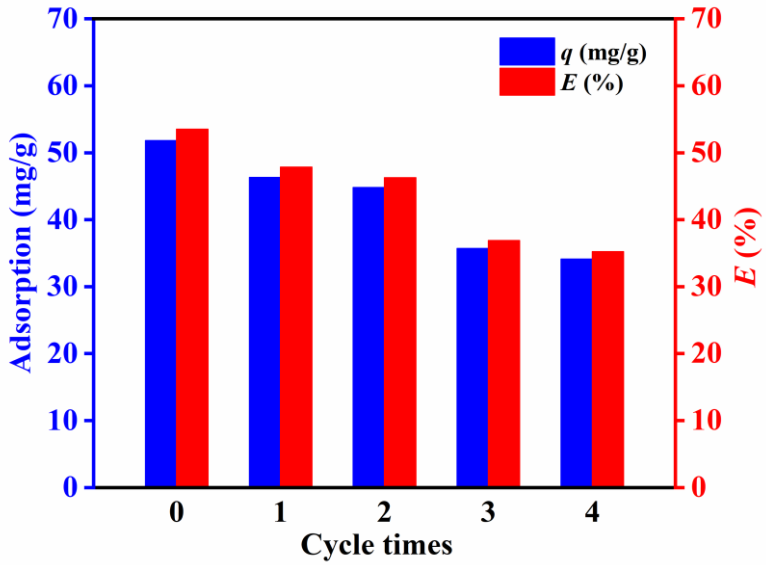

Figure 12. Sr^{2+} adsorption capacity and adsorption efficiency (*E*) of SA-PA-H hydrogel in batch adsorption experiments with an initial Sr^{2+} concentration of 100 ppm as a function of regeneration time. The SA-PA-H used was regenerated by washing the adsorbents with 100 mL 0.5 mol/L hydrochloric acid.

3.3.8 Comparison of adsorption performance

Table 3 compares the as-developed SA-based adsorbent with other reported absorbents. As shown, the SA-PA-H hydrogel is among the most effective Sr^{2+} adsorbents in terms of maximum adsorption capacity. Moreover, the SA-PA-H adsorbent can reach adsorption equilibrium by a fast uptake kinetics and it is also sufficiently flexible to be shaped or loaded to fit different devices. These features enabled its application in continuous water purification processes such as column

763 filtration and membrane filtration, where the contact time between contaminated water and the
764 adsorbent is very limited that the adsorbents with slow uptake kinetics fail to achieve good
765 purification. Although there are adsorbents having significantly high adsorption capacity and short
766 equilibrium time, they are mostly in form of powder, difficult to be applied in real water treatment
767 because of their low availability to be fitted into common purification devices and the difficulties
768 of post-treatment after adsorption (e.g. easily causing secondary pollution). Taking advantage of
769 excellent adsorption efficiency, good selectivity, good pH stability and outstanding modality, SA-
770 PA-H is a promising adsorbent candidate for real water treatment.
771

772 Table 3 Comparison of the adsorbent developed in this work with other Sr^{2+} adsorbents reported.

Adsorbent	State	q_{max} (mg/g)	Equilibrium (min)	pH range	Reference
Na Titanate	powder	49.6	60	3-10	[24]
polyantimonic acid-polyacrylonitrile (PAA-PAN)	powder	49	500	n. a.	[23]
Graphene oxide (GO)	powder	131.4	20	3-11	[22]
Covalent triazine polymer–Fe_3O_4 (CTP-Fe_3O_4)	powder	128	200	7-14	[31]
layered vanadosilicate (SGU-7)	powder	109	10	3-13	[57]
$Na_2Sn_3S_7$ (NaTS)	powder	80.0	1	3-13	[46]
$K_{1.87}ZnSn_{1.68}S_{5.30}$ (KZTS)	powder	19.3	1	3-11	[47]
$Na_5Zn_{3.5}Sn_{3.5}S_{13}\cdot 6H_2O$ (NaZTS)	powder	40.40	5	3-12	[49]
Impregnated nano-zeolite (NAASMS-Z)	powder	350	30	7-10	[26]
$K_2Sb_4S_7\cdot 2H_2O$ (SbS-1K)	powder	61.1	40	4-11	[58]
Thioglycolic acid-modified alginate sodium (SA-TGA)	microsphere	177.37	180	4–8	[44]
metakaolin/slag-based zeolite (M/SZMs)	microsphere	54.90	30	4-8	[59]
Chitosan	Fiber and microsphere	20.0	200	3-7	[60]
Graphene oxide/Nickel-metal-organic framework composite (GO/Ni-MOF)	membrane	72	>500	n.a.	[61]
Bacterial cellulose membrane modified with ethylenediaminetetraacetic acid (BCM@APTES-EDTA)	membrane	44.86	600	n.a.	[30]
SA-PA-H	moldable hydrogel	151.7	30	4-10	This work

773

4 Conclusion

A Sr^{2+}-imprinted and thiol-functionalized hydrogel based on SA (*i.e.* SA-PA-H) was successfully synthesized and used to selectively adsorb Sr^{2+} from contaminated water. The synthesis of hydrogel involved three steps including the formation of SA hydrogel in emulsion via complexation with Sr^{2+}, crosslinking of the alginate gels via esterification with thiol-functionalized tetra-arm carboxylic acids (PA), and lastly activation by acid elution to form Sr^{2+}-imprinted cavities. The synthesis route was verified by a series of techniques including NMR, FTIR, XPS and SEM, etc.

The incorporation of abundant thiol groups and the imprinted cavities with predetermined sizes endow the prepared SA-PA-H hydrogel with an excellent adsorption ability and decent selectivity towards Sr^{2+} within a wide range of pH (4-10) and temperature (25-40 °C). The adsorption process followed second-order kinetics at an adsorption rate constant of 0.669 g mg^{-1} min^{-1}. The isothermal adsorption behavior can be well described by the dual-site Langmuir model with a maximum adsorption capacity of 151.7 mg g^{-1}. The Sr^{2+} binding to thiol and carboxyl groups has been confirmed to be the two main adsorption mechanisms. The selectivity was validated by that the existence of competing ions such as Mg^{2+}, K^+ and Na^+ hardly weakened the adsorption efficiency of SA-PA-H to Sr^{2+}, having a K_d greater than 1.97×10^2 mL/g obtained even at high competing ion concentrations.

Rheological investigation reveals that SA-PA-H hydrogel can self-recover after being damaged by large strains. The hydrogel can be easily fabricated into membranes for Sr^{2+} separation with high removal efficiency (> 99.2%) within a wide range of liquid flux. The SA-PA-H adsorbent can be readily regenerated by washing with HCl solutions and the regenerated adsorbents possess comparable adsorption capability as the pristine hydrogel. The research developed a facile way to fabricate alginate-based hydrogel adsorbent for selective Sr^{2+} separation. Thanks to its outstanding adsorption capability and good mechanical properties, SA-PA-H is promising in strontium recovery for contaminated water treatment.

Acknowledgements

This research was financially supported by the National Natural Science Foundation of China (22172028; 21903015; and 22111530080), the Natural Science Foundation of Fujian Province of China (2020J01145 and 2022J05041), the Award Program of Fujian Minjiang Scholar Professorship (2018) and the European Union's "Horizon 2020" research and innovation programme under the Marie Skłodowska-Curie Grant Agreement No. 844286(M4WASTE).

Appendix A. Supplementary data

Supplementary data to this article can be found online at: XXXX

AUTHOR INFORMATION

Corresponding Authors

*E-mail: huagui.zhang@fjnu.edu.cn (H. Zhang)

Author Contributions

#B. Zheng and J. Yin contributed equally to this work.

Notes

The authors declare no competing interest.

Reference

[1] I. Smičiklas, M. Jović, M. Šljivić-Ivanović, V. Mrvić, D. Čakmak, S. Dimović, Correlation of Sr2+ retention and distribution with properties of different soil types, Geoderma 253-254 (2015) 21-29. 10.1016/j.geoderma.2015.04.003.

[2] Z. Begum, I. Rahman, T. Takase, H. Hasegawa, Formation and stability of the mixed-chelator complexes of Sr^{2+}, Mg^{2+}, Ca^{2+}, Ba^{2+}, and Y^{3+} in solution with bio-relevant chelators, J. Inorg. Biochem. 195 (2019) 141-148. https://doi.org/10.1016/j.jinorgbio.2019.03.018.

[3] Y. Li, S. Le, Z. Wang, Y. Hong, K. Li, Q. Pu, Preparation and characterization of the Sr^{2+}-doped γ-Ce_2S_3@c-SiO_2 red pigments exhibiting improved temperature and acid stability, Appl. Surf. Sci. 508 (2020) 145266-145273. https://doi.org/10.1016/j.apsusc.2020.145266.

[4] K. Xu, W. Chen, G. Fu, X. Mou, R. Hou, Y. Zhu, K. Cai, In situ self-assembly of graphene oxide/polydopamine/Sr2+ nanosheets on titanium surfaces for enhanced osteogenic differentiation of mesenchymal stem cells, Carbon 142 (2019) 567-579.

[5] J. Boonlakhorn, N. Chanlek, P. Thongbai, P. Srepusharawoot, Strongly enhanced dielectric response and structural investigation of (Sr2+, Ge4+) co-doped CCTO ceramics, J. Phys. Chem. C 124 (2020) 20682-20692.

[6] C. Chen, T. Xuan, W. Bai, T. Zhou, F. Huang, A. Xie, L. Wang, R. Xie, Highly stable CsPbI3: Sr2+ nanocrystals with near-unity quantum yield enabling perovskite light-emitting diodes with an external quantum efficiency of 17.1%, Nano Energy 85 (2021) 106033.

https://doi.org/10.1016/j.nanoen.2021.106033.

[7] X. Liu, Z. Ren, T. Yang, Y. Hao, Q. Wang, J. Zhou, Tunable dielectric metamaterial based on strontium titanate artificial atoms, Scripta Mater. 184 (2020) 30-33. https://doi.org/10.1016/j.scriptamat.2020.03.041.

[8] T. Su, Z. Han, Z. Qu, Y. Chen, X. Lin, S. Zhu, R. Bian, X. Xie, Effective recycling of Co and Sr from Co/Sr-bearing wastewater via an integrated Fe coagulation and hematite precipitation approach, Environ. Res. 187 (2020) 109654-109662. https://doi.org/10.1016/j.envres.2020.109654.

[9] S. Mane, S. Ponrathnam, N. Chavan, Selective solid-phase extraction of metal for water decontamination, J. Appl. Polym. Sci. 133 (2016) 42849. 10.1002/app.42849.

[10] H. Zhang, S. Tangparitkul, B. Hendry, J. Harper, Y.K. Kim, T.N. Hunter, J.W. Lee, D. Harbottle, Selective separation of cesium contaminated clays from pristine clays by flotation, Chem. Eng. J. 355 (2019) 797-804. 10.1016/j.cej.2018.07.135.

[11] J. Xu, H. Qiao, K. Yu, M. Chen, C. Liu, W. Richtering, H. Zhang, Cu^{2+} tunable temperature-responsive Pickering foams stabilized by poly (N-isopropylacrylamide-co-vinyl imidazole) microgel: Significance for Cu^{2+} recovery via flotation, Chem. Eng. J. 442 (2022) 136274. 10.1016/j.cej.2022.136274.

[12] L. Zhu, D. Zhu, Y. Sheng, J. Xu, D. Harbottle, H. Zhang, Polydopamine-coated magnetic montmorillonite immobilized with potassium copper hexacyanoferrate for selective removal of Cs+ and its facile recovery, Appl. Clay Sci. 216 (2022). 10.1016/j.clay.2021.106367.

[13] H. Zhang, C.S. Hodges, P.K. Mishra, J.Y. Yoon, T.N. Hunter, J.W. Lee, D. Harbottle, Bio-Inspired Preparation of Clay-Hexacyanoferrate Composite Hydrogels as Super Adsorbents for Cs(I), ACS Appl. Mater. Interfaces 12 (2020) 33173-33185. 10.1021/acsami.0c06598.

[14] C.R. Minitha, R. Suresh, U.K. Maity, Y. Haldorai, V. Subramaniam, P. Manoravi, M. Joseph, R.T. Rajendra Kumar, Magnetite Nanoparticle Decorated Reduced Graphene Oxide Composite as an Efficient and Recoverable Adsorbent for the Removal of Cesium and Strontium Ions, Ind. Eng. Chem. Res. 57 (2018) 1225-1232. https://doi.org/10.1021/acs.iecr.7b05340.

[15] Y.C. Zou, L. Mogg, N. Clark, C. Bacaksiz, S. Milovanovic, V. Sreepal, G.P. Hao, Y.C. Wang, D.G. Hopkinson, R. Gorbachev, S. Shaw, K.S. Novoselov, R. Raveendran-Nair, F.M. Peeters, M. Lozada-Hidalgo, S.J. Haigh, Ion exchange in atomically thin clays and micas, Nat. Mater. 20 (2021) 1677-1682. 10.1038/s41563-021-01072-6.

[16] E. Han, Y. Kim, H. Yang, I. Yoon, M. Choi, Synergy between zeolite framework and encapsulated sulfur for enhanced ion-exchange selectivity to radioactive cesium, Chem. Mater. 30 (2018) 5777-5785. http://doi.org/10.1021/acs.chemmater.8b02782.

[17] P. Khan, A. Bhattacharyya, J. Sharma, S. Manohar, The recovery of strontium from acidic medium using novel strontium selective extractant: An experimental and DFT study, J. Hazard. Mater. 397 (2020) 122476-122484. https://doi.org/10.1016/j.jhazmat.2020.122476.

[18] S. Younis, R. El-Salamony, Y. Tsang, K. Kim, Use of rice straw-based biochar for batch sorption of barium/strontium from saline water: protection against scale formation in petroleum/desalination industries, J. Clean. Prod. 250 (2020) 119442-119450. https://doi.org/10.1016/j.jclepro.2019.119442.

[19] H. Kim, Y. Kang, Y. Lee, S. Choi, J. Lim, J. Lee, Automated extraction chromatographic radionuclide separation system for analysis of ^{90}Sr in seawater, Talanta 217 (2020) 121055-

121063. https://doi.org/10.1016/j.talanta.2020.121055.

[20] M. Feng, D. Sarma, Y. Gao, X. Qi, W. Li, X. Huang, M.G. Kanatzidis, Efficient removal of $[UO_2]^{2+}$, Cs^+, and Sr^{2+} ions by radiation-resistant gallium thioantimonates, J. Am. Chem. Soc. 140 (2018) 11133-11140. https://doi.org/10.1021/jacs.8b07457.

[21] B. Park, S. Ghoreishian, Y. Kim, B. Park, S. Kang, Y. Huh, Dual-functional micro-adsorbents: application for simultaneous adsorption of cesium and strontium, Chemosphere 263 (2021) 128266-128275. https://doi.org/10.1016/j.chemosphere.2020.128266.

[22] A. Abu-Nada, A. Abdala, G. McKay, Isotherm and Kinetic Modeling of Strontium Adsorption on Graphene Oxide, Nanomaterials 11 (2021) 2780-2790. https://doi.org/10.3390/nano11112780.

[23] F. Ma, Z. Li, W. Zhou, Q. Li, L. Zhang, Application of polyantimonic acid–polyacrylonitrile for removal of strontium (II) from simulated high-level liquid waste, J. Radioanal. Nucl. Chem. 311 (2017) 2007-2013.

[24] C. Li, C. Liu, L. Chen, Z. Ye, Y. Zhang, X. Wang, Y. Wei, Studies on the separation and in-situ sintering solidification of strontium by a highly-efficient titanate-based adsorbent, .Micropors Mesopor. Mater. 288 (2019) 109607-109615. https://doi.org/10.1016/j.micromeso.2019.109607.

[25] S. Kwon, C. Kim, E. Han, H. Lee, H. Cho, M. Choi, Relationship between zeolite structure and capture capability for radioactive cesium and strontium, J. Hazard. Mater. 408 (2021) 124419. https://doi.org/10.1016/j.jhazmat.2020.124419.

[26] H. Hassan, O.A. Moamen, W. Zaher, Adaptive Neuro-Fuzzy inference system analysis on sorption studies of strontium and cesium cations onto a novel impregnated nano-zeolite, Adv. Powder Technol. 31 (2020) 1125-1139. https://doi.org/10.1016/j.apt.2019.12.031.

[27] T. Shubair, O. Eljamal, A. Tahara, Y. Sugihara, N. Matsunaga, Preparation of new magnetic zeolite nanocomposites for removal of strontium from polluted waters, J. Mol. Liq. 288 (2019) 111026-111036. https://doi.org/10.1016/j.molliq.2019.111026.

[28] N. Ghaeni, M.S. Taleshi, F. Elmi, Removal and recovery of strontium (Sr (II)) from seawater by Fe3O4/MnO2/fulvic acid nanocomposite, Mar. Chem. 213 (2019) 33-39.

[29] J. Choi, Y. Park, S. Choi, Synthesis of metal-organic framework ZnO_x-MOF@MnO_2 composites for selective removal of strontium ions from aqueous solutions, ACS Omega 5 (2020) 8721-8729. https://doi.org/10.1021/acsomega.0c00228.

[30] R. Cheng, M. Kang, S. Zhuang, L. Shi, X. Zheng, J. Wang, Adsorption of Sr (II) from water by mercerized bacterial cellulose membrane modified with EDTA, J. Hazard. Mater. 364 (2019) 645-653.

[31] A. Rengaraj, Y. Haldorai, P. Puthiaraj, S.K. Hwang, T. Ryu, J. Shin, Y.-K. Han, W.-S. Ahn, Y.S. Huh, Covalent Triazine Polymer–Fe3O4 Nanocomposite for Strontium Ion Removal from Seawater, Ind. Eng. Chem. Res. 56 (2017) 4984-4992. 10.1021/acs.iecr.7b00052.

[32] T. Lu, Y. Zhu, W. Wang, Y. Qi, A. Wang, Polyaniline-functionalized porous adsorbent for Sr2+ adsorption, J. Radioanal. Nucl. Chem. 317 (2018) 907-917. 10.1007/s10967-018-5935-9.

[33] S. Thakur, B. Sharma, A. Verma, J. Chaudhary, S. Tamulevicius, V.K. Thakur, Recent progress in sodium alginate based sustainable hydrogels for environmental applications, J. Clean. Prod. 198 (2018) 143-159. 10.1016/j.jclepro.2018.06.259.

[34] J. Yang, Y. Xie, W. He, Research progress on chemical modification of alginate: A review, Carbohydr. Polym. 84 (2011) 33-39. https://doi.org/10.1016/j.carbpol.2010.11.048.

[35] X. Gao, C. Guo, J. Hao, Z. Zhao, H. Long, M. Li, Adsorption of heavy metal ions by sodium alginate based adsorbent-a review and new perspectives, Int. J. Biol. Macromol. 164 (2020) 4423-4434.

[36] S.R. Choe, Y. Haldorai, S.-C. Jang, M. Rethinasabapathy, Y.-C. Lee, Y.-K. Han, Y.-S. Jun, C. Roh, Y.S. Huh, Fabrication of alginate/humic acid/Fe-aminoclay hydrogel composed of a grafted-network for the efficient removal of strontium ions from aqueous solution, Environ. Technol. Inno. 9 (2018) 285-293. https://doi.org/10.1016/j.eti.2017.12.008.

[37] S. Foster, N. Ramanan, B. Hanson, B. Mishra, Binding mechanism of strontium to biopolymer hydrogel composite materials, J. Radioanal. Nucl. Chem. (2022). https://doi.org/10.1007/s10967-022-08613-6.

[38] D. Fila, Z. Hubicki, D. Kołodyńska, Applicability of new sustainable and efficient alginate-based composites for critical raw materials recovery: General composites fabrication optimization and adsorption performance evaluation, Chem. Eng. J. 446 (2022). https://doi.org/10.1016/j.cej.2022.137245.

[39] A.S. Eltaweil, E.M. Abd El-Monaem, H.M. Elshishini, H.G. El-Aqapa, M. Hosny, A.M. Abdelfatah, M.S. Ahmed, E.N. Hammad, G.M. El-Subruiti, M. Fawzy, A.M. Omer, Recent developments in alginate-based adsorbents for removing phosphate ions from wastewater: a review, RSC Adv 12 (2022) 8228-8248. http://doi.org/10.1039/d1ra09193j.

[40] V. Kusumkar, M. Galambos, E. Viglasova, M. Dano, J. Smelkova, Ion-Imprinted Polymers: Synthesis, Characterization, and Adsorption of Radionuclides, Materials 14 (2021) 1083. https://doi.org/10.3390/ma14051083.

[41] L. Qin, Y. Zhao, L. Wang, L. Zhang, S. Kang, W. Wang, T. Zhang, S. Song, Preparation of ion-imprinted montmorillonite nanosheets/chitosan gel beads for selective recovery of Cu(II) from wastewater, Chemosphere 252 (2020) 126560. https://doi.org/10.1016/j.chemosphere.2020.126560.

[42] X. Luo, B. Guo, J. Luo, F. Deng, S. Zhang, S. Luo, J. Crittenden, Recovery of Lithium from Wastewater Using Development of Li Ion-Imprinted Polymers, ACS Sustainable Chemistry & Engineering 3 (2015) 460-467. 10.1021/sc500659h.

[43] D. Sun, Y. Zhu, M. Meng, Y. Qiao, Y. Yan, C. Li, Fabrication of highly selective ion imprinted macroporous membranes with crown ether for targeted separation of lithium ion, Sep. Purif. Technol. 175 (2017) 19-26. 10.1016/j.seppur.2016.11.029.

[44] C. Liu, X. Yu, C. Ma, Y. Guo, T. Deng, Selective recovery of strontium from oilfield water by ion-imprinted alginate microspheres modified with thioglycollic acid, Chem. Eng. J. 410 (2021) 128267. 10.1016/j.cej.2020.128267.

[45] R. Pearson, Hard and soft acids and bases, J. Am. Chem. Soc. 85 (1963) 3533-3539. https://doi.org/10.1021/ja00905a001.

[46] Z. Zhang, P. Gu, M. Zhang, S. Yan, L. Dong, G. Zhang, Synthesis of a robust layered metal sulfide for rapid and effective removal of Sr^{2+} from aqueous solutions, Chem. Eng. J. 372 (2019) 1205-1215. https://doi.org/10.1016/j.cej.2019.04.193.

[47] M. Zhang, P. Gu, Z. Zhang, J. Liu, L. Dong, G. Zhang, Effective, rapid and selective adsorption of radioactive Sr2+ from aqueous solution by a novel metal sulfide adsorbent, Chem. Eng. J. 351 (2018) 668-677. 10.1016/j.cej.2018.06.069.

[48] Y.M. Zhao, M. Sun, L. Cheng, K.Y. Wang, Y. Liu, J.Y. Zhu, S. Zhang, C. Wang, Efficient removal of Ba(2+), Co(2+) and Ni(2+) by an ethylammonium-templated indium sulfide ion

exchanger, J. Hazard. Mater. 425 (2022) 128007. https://doi.org/10.1016/j.jhazmat.2021.128007.

[49] M. Zhang, P. Gu, S. Yan, L. Dong, G. Zhang, Na/Zn/Sn/S (NaZTS): Quaternary metal sulfide nanosheets for efficient adsorption of radioactive strontium ions, Chem. Eng. J. 379 (2020). 10.1016/j.cej.2019.122227.

[50] W. Mu, S. Du, Q. Yu, X. Li, H. Wei, Y. Yang, S. Peng, Highly efficient removal of radioactive ^{90}Sr based on sulfonic acid-functionalized α-zirconium phosphate nanosheets, Chem. Eng. J. 361 (2019) 538-546. https://doi.org/10.1016/j.cej.2018.12.110.

[51] A. James, S. Harding, T. Robshaw, N. Bramall, M. Ogden, R. Dawson, Selective environmental remediation of strontium and cesium sing sulfonated hyper-cross-linked polymers (SHCPs), ACS Appl. Mater. Inter. 11 (2019) 22464-22473. https://doi.org/10.1021/acsami.9b06295.

[52] S. Kalam, S.A. Abu-Khamsin, M.S. Kamal, S. Patil, Surfactant Adsorption Isotherms: A Review, ACS Omega 6 (2021) 32342-32348. http://doi.org/10.1021/acsomega.1c04661.

[53] G.D. Değermenci, N. Değermenci, V. Ayvaoğlu, E. Durmaz, D. Çakır, E. Akan, Adsorption of reactive dyes on lignocellulosic waste; characterization, equilibrium, kinetic and thermodynamic studies, J. Clean. Prod. 225 (2019) 1220-1229. http://doi.org/10.1016/j.jclepro.2019.03.260.

[54] A. Zapata-Sierra, M. Cascajares, A. Alcayde, F. Manzano-Agugliaro, Worldwide research trends on desalination, Desalination 519 (2021) 115305. 10.1016/j.desal.2021.115305.

[55] H. Zhang, S. Zhu, J. Yang, A. Ma, W. Chen, Enhanced removal efficiency of heavy metal ions by assembling phytic acid on polyamide nanofiltration membrane, Journal of Membrane Science 636 (2021) 119591. 10.1016/j.memsci.2021.119591.

[56] H. Xiang, X. Min, C. Tang, M. Sillanpää, F. Zhao, Recent advances in membrane filtration for heavy metal removal from wastewater: A mini review, J. Water Process Eng. 49 (2022) 103023. https://doi.org/10.1016/j.jwpe.2022.103023.

[57] S. Datta, P. Oleynikov, W. Moon, Y. Ma, A. Mayoral, H. Kim, C. Dejoie, M. Song, O. Terasaki, K. Yoon, Removal of ^{90}Sr from highly Na^{+}-rich liquid nuclear waste with a layered vanadosilicate, Energ. Environ. Sci. 12 (2019) 1857-1865. https://doi.org/10.1039/C8EE03302A.

[58] Y. Zhao, L. Cheng, K. Wang, X. Hao, J. Wang, J. Zhu, M. Sun, C. Wang, pH-Controlled Switch over Coadsorption and Separation for Mixed Cs^{+} and Sr^{2+} by an Acid-Resistant Potassium Thioantimonate, Adv. Funct. Mater. 32 (2022) 2112717. https://doi.org/10.1002/adfm.202112717.

[59] H. Lei, Y. Muhammad, K. Wang, M. Yi, C. He, Y. Wei, T. Fujita, Facile fabrication of metakaolin/slag-based zeolite microspheres (M/SZMs) geopolymer for the efficient remediation of Cs^{+} and Sr^{2+} from aqueous media, J. Hazard. Mater. 406 (2021) 124292. 10.1016/j.jhazmat.2020.124292.

[60] S. Zhuang, K. Zhu, L. Xu, J. Hu, J. Wang, Adsorption of Co^{2+} and Sr^{2+} in aqueous solution by a novel fibrous chitosan biosorbent, Sci. Total Environ. 825 (2022) 153998. 10.1016/j.scitotenv.2022.153998.

[61] J. Cheng, K. Liu, X. Li, L. Huang, J. Liang, G. Zheng, G. Shan, Nickel-metal-organic framework nanobelt based composite membranes for efficient Sr^{2+} removal from aqueous solution, Environmental Science and Ecotechnology 3 (2020) 100035.

10.1016/j.ese.2020.100035.